Sensitivity to Surface Forcing and Boundary Layer Mixing in a Global Ocean Model: Annual-Mean Climatology

WILLIAM G. LARGE, GOKHAN DANABASOGLU, AND SCOTT C. DONEY

National Center for Atmospheric Research, Boulder, Colorado

JAMES C. MCWILLIAMS

Department of Atmospheric Sciences, University of California, Los Angeles, Los Angeles, California

(Manuscript received 8 November 1996, in final form 17 April 1997)

ABSTRACT

The effects of more realistic bulk forcing boundary conditions, a more physical subgrid-scale vertical mixing parameterization, and more accurate bottom topography are investigated in a coarse-resolution, global oceanic general circulation model. In contrast to forcing with prescribed fluxes, the bulk forcing utilizes the evolving model sea surface temperatures and monthly atmospheric fields based on reanalyses by the National Centers for Environmental Prediction and on satellite data products. The vertical mixing in the oceanic boundary layer is governed by a nonlocal K-profile parameterization (KPP) and is matched to parameterizations of mixing in the interior. The KPP scheme is designed to represent well both convective and wind-driven entrainment. The near-equilibrium solutions are compared to a baseline experiment in which the surface tracers are strongly restored everywhere to climatology and the vertical mixing is conventional with constant coefficients, except where there is either convective or near-surface enhancement.

The most profound effects are due to the bulk forcing boundary conditions, while KPP mixing has little effect on the annual-mean state of the ocean model below the upper few hundred meters. Compared to restoring boundary conditions, bulk forcing produces poleward heat and salt transports in better agreement with most oceanographic estimates and maintains the abyssal salinity and temperature closer to observations. The KPP scheme produces mixed layers and boundary layers with realistically large temporal and spatial variability. In addition, it allows for more near-surface vertical shear, particularly in the equatorial regions, and results in enhanced large-scale surface divergence and convergence. Generally, topographic effects are confined locally, with some important consequences. For example, realistic ocean bottom topography between Greenland and Europe locks the position of the sinking branch of the Atlantic thermohaline circulation to the Icelandic Ridge. The model solutions are especially sensitive to the under-ice boundary conditions where model tracers are strongly restored to climatology in all cases. In particular, a factor of 4 reduction in the strength of under-ice restoring diminishes the abyssal salinity improvements by about 30%.

1. Introduction

The history, formulation, and solutions of ocean general circulation models (OGCMs) have been reviewed comprehensively by McWilliams (1996). Among the topics discussed in detail are three that are relevant here, namely, surface boundary conditions, subgrid-scale vertical mixing, and domain geometry. The review concludes with the view that more realistic, less constraining surface boundary conditions are the most likely prospect for obtaining novel OGCM solutions. Furthermore, it is noted that OGCM solutions are sensitive to their subgrid-scale vertical tracer (heat and salt) diffusivity. For example, the thickness of the main pycnocline varies as the square root of the vertical tracer diffusivity (e.g., Salmon 1990). However, Bryan (1987) found that for his model physics a realistic pycnocline and poleward heat transport are incompatible, with the former requiring a smaller diffusivity than the latter. In addition, McWilliams (1996) places the desire to model the complex, rough ocean bottom and coastline of physical reality in competition with the simple, smooth topography needed to assure numerical accuracy.

A common OGCM boundary condition is to restore the surface tracer values to observed climatology, with a time constant that ranges from days to months (e.g., Cox and Bryan 1984; Danabasoglu and McWilliams 1995). Such a formulation precludes the possibility of having nonzero flux coincident with correct model surface tracer fields, and spatial variability in the tracer flux fields, especially freshwater, becomes excessive with shorter time constants. Often, the specified climatology and time constant vary with time and space

Corresponding author address: Dr. William G. Large, NCAR, P.O. Box 3000, Boulder, CO 80307.
E-mail: wily@leon.cgd.ucar.edu

and are designed to give observed surface fluxes when surface tracer values match observations (e.g., Haney 1971; Han 1984). Alternative flux boundary conditions are usually employed for momentum and can be used for tracers by specifying the net heat and freshwater fluxes everywhere over the model domain. However, the sea surface temperature (SST) of OGCMs forced with specified tracer fluxes often evolves far from the observed surface temperature used to compute the fluxes (Rosati and Miyakoda 1988). This physical inconsistency is due to the lack of air–sea feedbacks, which can be overcome by bulk forcing where the uppermost model temperature is equated to SST in the bulk formulas used to compute the fluxes. For example, Hirst and Godfrey (1993) and Oberhuber (1993) employ bulk thermal forcing but do not link the heat and freshwater fluxes through evaporation. Ocean variability studies have successfully employed mixed tracer boundary conditions where the surface temperature is restored, but the freshwater flux is specified, usually as diagnosed from a restored salinity experiment (e.g., Tziperman et al. 1994).

A major advance in the observational database is the routine production of all the surface fluxes and flux parameters by the Numerical Weather Prediction centers such as the National Centers for Environmental Prediction (NCEP) and the European Center for Medium-Range Weather Forecasts (ECMWF). Barnier et al. (1995) review thermal forcing of OGCMs and formulate a thermal boundary condition based on ECMWF analyses. Three years of these data are used to compute climatologies of SST and net heat flux. Standard bulk formulas express the net heat flux as a function of SST. Their net surface heat flux is then given by a two-term Taylor series expansion of this function at all locations. The second term of this expansion is similar to the Haney (1971) and Han (1984) thermal forcing.

Subgrid-scale vertical mixing is usually parameterized as downgradient diffusion and often, particularly at depth, the vertical eddy diffusivity and viscosity are constant. In addition, some means of relieving gravitationally unstable density stratification is usually provided. Two popular schemes are substantial enhancement of the vertical diffusivity in unstable regions and convective adjustment. In the latter there is instantaneous mixing of all tracers until marginal stability is achieved. However, it is known that boundary layers have distinctive physics (Wyngaard 1982) and hence require their own mixing rules. In OGCMs the oceanic boundary layer is sometimes implicitly confined to the uppermost model level by applying interior mixing rules at all other depths. However, Chen et al. (1994) find that resolving boundary layer mixing in the upper layers of a tropical ocean improves the large-scale equatorial circulation as well as the amplitude and phase of the annual cycle of SST.

An OGCM cannot resolve all the topographic features of the ocean bottom and coastline, necessitating compromises. It is unclear which topographic features an OGCM should strive to represent most faithfully, although sill depth and cross-sectional area for passages with strong flows are likely to be of importance. If the width is too near the horizontal grid scale, the flow experiences excessive viscous damping due to no-slip side boundary conditions. Common practice is to widen important straits until at least four active velocity grid points are included. For example, a single, 4–5 gridpoint wide Indonesian Channel often connects the Pacific and Indian Oceans. The dramatic consequences of not having this passage in a global OGCM are shown by Hirst and Godfrey (1993). Drake Passage is another critical strait, whose width is sometimes doubled in coarse-resolution models (e.g., Toggweiler et al. 1989; Danabasoglu and McWilliams 1995). Although the Strait of Gibraltar is the source of saline Mediterranean Water, complete closure is often preferred to the excessive enlargement required to satisfy resolution issues (e.g., Hirst and Godfrey 1993; Danabasoglu and McWilliams 1995). Analogous problems are associated with the flow over sills and ridges, such as the Icelandic Ridge between Greenland and Europe.

The hypothesis guiding the present work is that more realistic and less constraining surface boundary conditions, more physical subgrid-scale vertical mixing, including boundary layer processes, and more accurate domain geometry and topography will result in improved equilibrium OGCM solutions. The strategy is to advance the OGCM of Danabasoglu and McWilliams (1995), hereafter referred to as DM95, to document any improvements and to isolate their cause. Although this work is ongoing, some significant progress is reported here. Of particular interest are equilibrium, climate relevant, annual-mean quantities such as water mass formation, the poleward transport of heat and freshwater, the thermohaline circulation, and the distributions of temperature and salinity especially at depth.

DM95 is similar to many previous coarse-resolution models, apart from its mesoscale tracer transport parameterization (Gent and McWilliams 1990). The major differences between our baseline integration and DM95 are the latitudinal resolution and topography, so the effects of the domain modifications can be examined. Other differences are detailed in section 2. In the baseline, referred to as R–E for restoring boundary conditions and enhanced mixing, there is strong restoring of surface temperature and salinity everywhere, and the vertical eddy diffusivity and viscosity are constants, except above 50-m depth and in regions of gravitational instability where they are greatly enhanced. This baseline is extensively compared to other near-equilibrium solutions where more realistic bulk forcing based on NCEP reanalysis and satellite data products is employed, except under diagnosed sea ice, and where the K-profile parameterization (KPP; section 4) of Large et al. (1994) governs vertical mixing in both the oceanic boundary layer and interior. Whenever the effects of KPP and bulk forcing, including under sea ice restoring, need to be distinguished, the near-equi-

TABLE 1. Summary of forcing in the numerical experiments and uncertainties due to not reaching absolute equilibrium. Units of the restoring coefficients for heat flux, Γ_Q, and freshwater fluxes, Γ_F and Γ_w, are W m^{-2} K^{-1} and mg m^{-2} s^{-1} ppt^{-1}, respectively. Sea ice formation and melt are enabled with $f_{si} = 1.0$ and disabled with $f_{si} = 0.0$. The precipitation adjustment factors used throughout the synchronous integrations are given as $f_P(960)$. Estimates of maximum expected drift during an additional 100 years of synchronous integration are given as $\delta\theta_{max}$ and δS_{max} (in units of °C and ppt).

	Γ_Q	Γ_F	f_{si}	Γ_w	$f_P(960)$	$\delta\theta_{max}$	δS_{max}
R–E	93	665	1.0	0	—	−0.0082	−0.0006
R–K	93	665	1.0	0	—	0.0040	0.0003
B–K$_1$	93	665	1.0	23	1.1085	−0.0250	0.0026
B–K	386	2770	1.0	23	1.1050	0.0675	0.0077
B–K$_2$	386	2770	0.0	23	1.1140	0.0321	0.0025
B–E	386	2770	1.0	23	1.1080	0.1301	0.0188

librium solutions of several variants are examined. One case, R–K, uses the restoring of the baseline and KPP mixing. In the other variants the bulk forcing differs in the strength of the under ice restoring and whether or not sea ice is allowed to form and melt locally. A total of six equilibrium solutions have been obtained within the computational resources allocated for this study. The forcing, including variations, are detailed in section 3 and summarized in Table 1.

2. Model configuration and parameters

a. Resolution, geometry, and topography

The model domain is global, extending from 80.1°S to 90°N. The longitudinal resolution of the model is constant at 3.6°. The latitudinal resolution is variable. Near the equator, it is 1.8° to better resolve the equatorial currents. Away from the equator it increases to a maximum of 3.4°, then decreases in the midlatitudes as the cosine of latitude to maintain horizontally uniform (isotropic) grid boxes. It is kept constant at 1.8° poleward of 60° to prevent any additional restrictions on the model time step. The maximum model depth is 5000 m, and there are 25 vertical levels, monotonically increasing in thickness from 12 m near the surface to 450 m near the bottom. The minimum model depth restriction is relaxed from the 2500 m of DM95 to 49 m, corresponding to 3 vertical levels and allowing for more realistic sill depths of the Icelandic Ridge and Drake Passage. The present model resolution is somewhat finer (7400 horizontal grid points) than the 4° × 3° × 20 level resolution used in DM95 (5400 horizontal grid points).

The land boundaries used in the present study are shown in Fig. 1. The Indonesian Channel, the Florida Straits, and the connections to the Sea of Japan are much wider than in reality. The present 9.4°-wide Drake Passage closely matches the actual width of the passage. Antarctica, Australia, Cuba/Hispaniola, Iceland, Japan, Madagascar, New Zealand, and Spitsbergen are the only islands in the model. In contrast, in DM95 Antarctica, Australia, and the North Pole are the only islands, and the Drake Passage is 15° wide. However, similar to DM95, Greenland is connected to North America. Also, the Bering and Gibraltar Straits and the Red Sea outflow are closed, with potential consequences for the properties of the Arctic, Atlantic, and Indian Ocean basins, respectively.

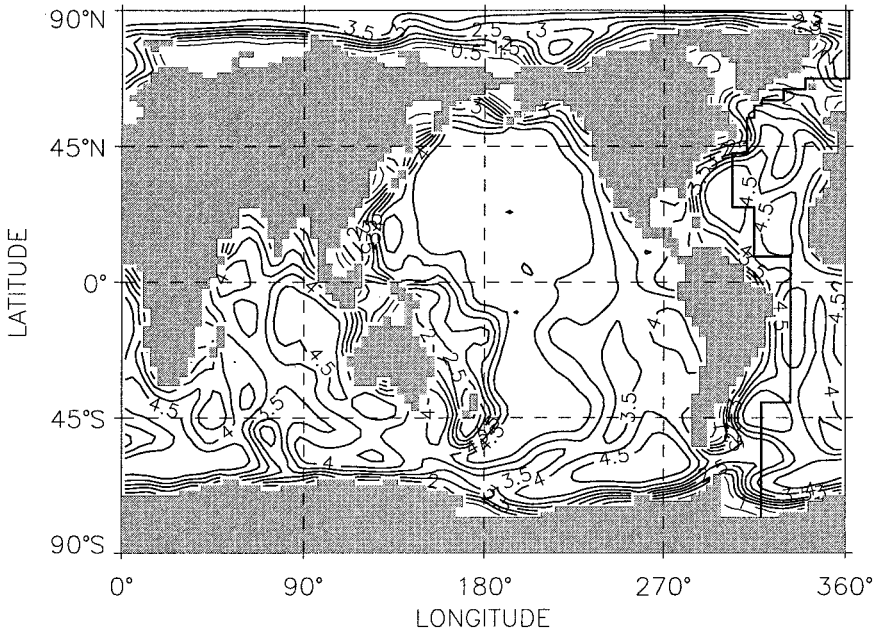

FIG. 1. Continental outlines and bottom topography of the model. Depth contours are 0.5-km intervals. Thinner lines are used for 0.5-km and 1-km contour levels. The thick, solid, vertical line segments mark the center of the meridional sections through the Atlantic Ocean used in Fig. 5.

The bottom topography of the model is based on the data from the NOAA National Geophysical Data Center (Sloss 1988). After obtaining the topography on the present model grid, several modifications are done to prevent numerical instabilities and inaccuracies associated with topographic roughness. First, a local, five-point Gaussian filter is applied five times to smooth the bottom topography (Fig. 1). The advectively isolated holes at depth, usually with one-gridpoint spatial extents, are then filled. To preserve smoothness, three points in the Denmark Strait are lowered by one grid level, and one point southeast of Iceland is raised by one grid level. Nevertheless, the topography of the Denmark Strait and Faroe–Iceland Ridge is realistic with maximum depths of 734 and 903 m, respectively. Finally, the North Pole point and the grid points immediately south of it are artificially adjusted to have a depth of 3680 m.

b. Model description and parameters

The governing equations of the oceanic general circulation model are the primitive equations in spherical coordinates, with the hydrostatic, Boussinesq, and rigid-lid approximations. The model is based on the Modular Ocean Model (MOM 1.1) of the Geophysical Fluid Dynamics Laboratory (GFDL) (Bryan 1969; Cox 1984; Pacanowski et al. 1991, 1993). In addition to a single vertical velocity computation, Danabasoglu et al. (1994) and DM95 add the isopycnal transport parameterization of Gent and McWilliams (1990) and extensively study its effects on OGCMs. The most important additional features implemented for the present study are KPP vertical mixing (section 4), surface bulk forcing (section 3; appendix A), sea ice formation (section 3), and additional tapering functions used in the isopycnal transport parameterization (appendix B). Others include treatment of the North Pole as an active tracer point, ability to taper horizontal viscosity and isopycnal diffusion coefficients to obey viscous stability limits, and inclusion of additional viscous terms in the momentum equations to preserve solid body rotation (Wajsowicz 1993). This line of model development continues as the NCAR (National Center for Atmospheric Research) Climate System Model (CSM) Ocean Model and the complete suite of modifications/improvements, including those implemented subsequent to the current study, is detailed in NCAR Oceanography Section (1996).

In all the numerical experiments, the horizontal eddy viscosity A_{MH}, horizontal eddy diffusion $A_{\tau H}$, isopycnal diffusion A_I, and thickness diffusion A_{ITD} coefficients are formulated identically. Numerical values are $A_{MH} = 3.0 \times 10^5$ (a factor of 3 smaller than DM95), $A_{\tau H} = 0$ [as allowed with the Gent and McWilliams (1990) parameterization], and $A_I = A_{ITD} = 0.8 \times 10^3$ m^2 s^{-1}. Here A_{MH} is chosen to allow resolution of the lateral viscous boundary layer (Munk 1950) and to limit the two-gridpoint noise in the barotropic streamfunction, which is integrated using the five-point conjugate gradient algorithm with sufficiently small convergence limit (Derber 1987): A_I and A_{ITD} are determined from observed (isobaric) float dispersion (Freeland et al. 1975; McWilliams et al. 1983), from sensitivity of some integrated model transports, especially the Antarctic Circumpolar Current transport (DM95), and from diagnoses of much higher resolution models (Rix and Willebrand 1996). They are both set to 1.0×10^3 m^2 s^{-1} in the primary case (I1) of DM95. Also, a quadratic bottom drag is used with a dimensionless drag coefficient of 1.0×10^{-3}. To relax the severe restriction on the length of time step allowed for advective numerical stability due to converging meridians toward the North Pole, the flow variables are Fourier filtered north of 75°N (Holloway et al. 1973). No filtering is used in the Southern Hemisphere. Although the Fourier filter preserves the mean of a transformed variable and reduces its variance along a latitude line at constant depth, the spatial redistribution of the variable in longitude may be different at neighboring latitudes and depths. Thus, filtering may contribute to small spatial-scale variability seen in the Arctic. A second restriction on model time step at high latitudes is due to the viscous/diffusive computational stability limit. Consequently, A_{MH} is tapered north of 81.9°N, using the viscous stability equation. North of 87.3°N, A_{MH} is kept constant at 0.6×10^5 m^2 s^{-1}. At all latitudes A_I and A_{ITD} satisfy this constraint without tapering. The vertical diffusion terms are treated implicitly.

As in DM95, the time integration is performed in two stages, both with a 3504 s time step for the momentum and barotropic streamfunction integrations. First, the acceleration technique of Bryan (1984) is used to accelerate the convergence to equilibrium in the abyssal ocean. In this accelerated phase, the tracer time step is larger by factors of 10 above 1099 m, 50 between 1099 m and 2510 m, and 100 below 2510 m. Thus, the upper- and deep-ocean tracer time steps are about 0.4 and 4 days, respectively. All experiments are accelerated for 96 momentum years, 960 surface tracer years, or 9600 deep tracer years. In the second stage, these integrations are continued for 30 years with equal (synchronous) time steps of 3504 s for all equations at all depths. The annual-mean fields from the last synchronous year, sampled every 15.21 days, are presented in sections 5 and 6.

Danabasoglu et al. (1996) present a detailed analysis of this time integration procedure, including the effects of unequal time steps and the requirements for equilibrium. They find the vertical tracer diffusion to have the longest timescale and recommend an accelerated integration of 6000 deep tracer years followed by 15 synchronous years. At the completion of our 50% longer accelerated integrations the temporal trends in the deep ocean salinity and potential temperature of each ocean basin are only about 1×10^{-6} °C yr^{-1} and 1×10^{-6} ppt yr^{-1}, respectively, so practical equilibrium is attained. But during the synchronous phase only near-

equilibria are reached, because the change in the surface tracer time step results in further adjustments that do not completely disappear in 30 years. Therefore, the annual-mean fields from the last three synchronous years are used to estimate the maximum drifts in potential temperature θ and salinity S that might occur over an additional 100 years of synchronous integration. Such estimates from the model level at 3474-m depth are computed globally and for each basin (excluding the Arctic, which has very little volume at this level). For each case, Table 1 gives the values for the basin with the largest possible 100-yr change, as $\delta\theta_{\max}$ and $\delta S_{\max}$. This basin is the Atlantic in all cases except for B-K_1 where the Southern Ocean has the largest trend estimate. In all cases the change estimates for the global average at 3474 m are at least a factor of 3 smaller for both θ and S.

The adjustments during the synchronous integrations diminish systematically with time, so very small trends would be expected after an additional 100 years. Therefore, $\delta\theta_{\max}$ and $\delta S_{\max}$ entries in Table 1 serve as a measure of the uncertainty in level averages of θ and S due to the solutions not being in perfect equilibrium at the end of the synchronous integration. As in DM95, this uncertainty is very small in the restoring cases. However, it is considerably larger in the other cases, but still small compared to case-to-case differences (sections 5 and 6).

3. Surface boundary conditions

The form of the forcing of the two restoring cases, R–E and R–K, is identical to that of DM95. However, DM95 restores to two annual harmonics and the present cases to midmonth climatologies (appendix A). The surface boundary conditions of the momentum equations are the zonal and meridional wind stresses. Everywhere, the only component of the net surface heat and freshwater fluxes is a strong restoring denoted by subscript (s):

$$Q = Q_s = \Gamma_Q(\theta_{STR} - \theta_1),$$
$$F = F_s = -\Gamma_F(S_L - S_1), \tag{3.1}$$

where θ_1 and S_1 are the model's evolving upper-layer potential temperature and salinity, and θ_{STR} and S_L are the corresponding annual cycles of climatological SST and salinity from Shea et al. (1990) and from Levitus (1982), respectively (appendix A). The restoring coefficients (Table 1) can be interpreted either as a 25-day restoring timescale over the upper 50 m of enhanced mixing, or a 6-day timescale over the thickness of the upper model level (12 m). Monthly fields of wind stress components, θ_{STR}, and S_L are linearly interpolated to each model time step, and details of how these fields are constructed are given in appendix A.

In the bulk forcing cases of Table 1 the wind forcing remains unchanged. Because the ocean model is not yet coupled to an explicit sea ice model, strong restoring in temperature and salinity is applied under sea ice. A fractional coverage of sea ice f_{ice} is diagnosed from the Shea et al. (1990) SST climatology, as detailed in appendix A. The bulk net surface heat and freshwater fluxes, with all components defined to be positive downward, then become

$$Q = (1 - f_{\text{ice}})Q_{\text{as}} + f_{\text{si}}Q_{\text{si}} + f_{\text{ice}}Q_{\text{s}}$$
$$F = (1 - f_{\text{ice}})F_{\text{as}} + f_{\text{si}}F_{\text{si}} + f_{\text{ice}}F_{\text{s}} + (1 - f_{\text{ice}})F_w, \tag{3.2}$$

where the usual air–sea fluxes, Q_{as} and F_{as}, and a weak salinity restoring, F_w, are applied only to diagnosed open (ice free) water. Fluxes associated with local sea ice formation and melt, Q_{si} and F_{si}, can occur anywhere provided these processes are enabled by setting $f_{\text{si}} = 1$. Strong under-ice restoring is fully applied only under complete ice coverage, $f_{\text{ice}} = 1$. Under partial coverage ($0 < f_{\text{ice}} < 1$) it is combined with the air–sea fluxes according to (3.2), so that there is a smooth transition from completely ice free to fully ice covered regions.

With bulk forcing the air–sea fluxes are the most important heat and freshwater forcing, because they dominate over more than 90% of the ocean's surface. These fluxes are as similar as is practical to the coupled forcing between the ocean model and an active atmospheric model (Bryan et al. 1996):

$$Q_{\text{as}} = Q_{\text{sen}} + Q_{\text{lat}} + Q_{\text{lw}} + Q_{\text{sw}},$$
$$F_{\text{as}} = P + E. \tag{3.3}$$

Details of the computation of precipitation P; of the turbulent fluxes of sensible heat Q_{sen}, latent heat Q_{lat}, and evaporation E; and of the net solar Q_{sw}, and longwave Q_{lw}, radiative heat fluxes are given in appendix A. The prognostic model temperature θ_1 is equated to SST in the empirical bulk formulas for the air–sea fluxes (3.3). Like the wind stress components, most of the other air–sea flux parameters are derived from the 6-hourly NCEP reanalyses (Kalnay et al. 1996) for the years 1985–88. However, various satellite data products are used for cloud fraction and solar radiation (ISCCP; Bishop and Rossow 1991; Rossow and Schiffer 1991) and precipitation (MSU; Spencer 1993).

With bulk forcing the possibility exists for the air–sea heat flux, when applied over a time interval δt, to produce regions of subfreezing model upper-layer temperatures. This condition is relieved by applying additional surface fluxes over the time interval that can be associated with the formation of sea ice. These fluxes are computed everywhere as

$$Q_{\text{si}} = c_p\rho_o(\theta_f - \theta_1)\Delta z_1\delta t^{-1},$$
$$F_{\text{si}} = -Q_{\text{si}}L_f^{-1}, \tag{3.4}$$

where $L_f = 334\,000$ J kg^{-1} is the latent heat of fusion, $c_p = 3996$ J kg^{-1} K^{-1} is the heat capacity of sea water,

TABLE 2. Global- and annual-mean heat and freshwater component fluxes from diagnostic SST calculations using θ_{STR} and from the equilibrium B–K case using θ_1. Averaging is performed over the total model ocean area (total area = 3.523×10^8 km^2, ice free area = 3.285×10^8 km^2). The heat and freshwater fluxes are in watts per square meter and meters per year.

	θ_{STR}		θ_1
	Original	Adjusted	(B–K)
Q_{sw}	172.0	150.6	150.6
Q_{lw}	−47.2	−49.1	−49.1
Q_{lat}	−73.3	−92.2	−91.3
Q_{sen}	−8.3	−8.3	−8.8
Q_{si}	—	—	−1.4
Q	43.2	1.0	0.0
E	−0.925	−1.163	−1.152
P	1.027	1.163	1.138
F_{si}	—	—	0.014
F	0.102	0.000	0.000

$\rho_o = 1026$ kg m^{-3} is the sea water density, $\theta_f = -1.8$°C approximates the freezing point of sea water, and $\Delta z_1 = 12$ m is the thickness of the uppermost model level. Thus any subfreezing surface water is immediately heated to the freezing point with a corresponding salinity increase. The associated sea ice is accumulated locally, but is not transported and effects neither f_{ice} nor the air–sea fluxes. If model-generated sea ice is present it keeps the surface temperature at freezing by making Q_{si} negative in (3.4) until it is all melted. Such melt also decreases the surface salinity according to $F_{si} > 0$ in (3.4). Because of vertical mixing, allowing deeper layers to freeze has little impact on the model solutions.

Of all the fluxes, the precipitation rates over the ocean are generally the most poorly known. Precipitation errors in bulk forcing could lead to unbounded local salinity trends. Therefore, the Levitus (1982) salinity climatology is used to provide some local constraint. Specifically, a local weak restoring freshwater flux F_w with zero global mean is applied over ice free regions (3.2). It is computed from (3.1), but with a weak coefficient Γ_w, that corresponds to a 2-yr restoring timescale over 12 m (Table 1). At every time step the global mean over the ice free ocean is subtracted so that F_w does not contribute to the global salinity budget.

Considerable uncertainty is associated with current air–sea heat and freshwater flux estimates (Weller and Taylor 1993). Appendix A describes how our atmospheric climatology has been adjusted, within acceptable error ranges, to generate globally balanced heat and freshwater budgets for an ocean with climatological sea surface temperature θ_{STR}.

a. Bulk forcing variants

Each model run is initialized with the January-mean Levitus θ and S fields, then integrated to near equilibrium at which time there are essentially zero net surface fluxes (Table 2) and little drift (Table 1). The first variant of bulk forcing (B–K$_1$) differs from the baseline R–E in its use of both KPP and bulk forcing. Even though the strong under-ice restoring coefficients are unchanged, the fluxes into the ice-covered Arctic Ocean are different. The choice is whether to keep the under-ice restoring coefficients constant or to make the fluxes more alike.

In order to investigate this issue, consider the annual-mean equilibrium surface fluxes in two circumpolar latitude bands; 80° to 87°N and 75° to 80°N. Over the more northern band the net freshwater flux is −22.1, −13.7, and −11.6 mg m^{-2} s^{-1} in cases R–E, R–K, and B–K$_1$, respectively, while the respective freshwater gains over the southern band are 31.5, 22.4, and 20.2 mg m^{-2} s^{-1}. First compare the cases with identical under-ice restoring coefficients; R–E and R–K (Table 1). There is a similar reduction in the surface cooling over these latitudes. The smaller heat and freshwater flux magnitudes of R–K are indicative of smaller property differences in (3.1). The use of bulk air–sea fluxes over the ice free ocean in B–K$_1$ leads to a further reduction in the freshwater flux magnitudes over both latitude bands. However, the Arctic fluxes can be made more compatible with R–E by increasing the under-ice restoring coefficients of bulk forcing. For example, a fourfold increase in both Γ_Q and Γ_F results in average freshwater fluxes of −15.0 and 25.5 mg m^{-2} s^{-1} in the above two latitude bands, respectively. There is also an increase in the cooling over the southern band, where the contribution to the buoyancy flux from the heat flux is nearly 50% that of the freshwater flux. In the northern band the effect on the cooling is mixed, but unimportant because the heat flux makes a negligible contribution to the buoyancy.

Since a major purpose is to isolate and evaluate the effects of bulk forcing over the ice free ocean, it can be argued that the more similar the under-ice fluxes the more meaningful the comparison. Therefore, the case with four times larger restoring coefficients (B–K; Table 1) is chosen for the most detailed comparison with R–E, and as a basis for two other experiments (Table 1). In case B–E, the KPP mixing of B–K is replaced with the enhanced vertical mixing of R–E so that the effects of KPP can be assessed cleanly. Experiment B–K$_2$ is identical to B–K except the sea ice formation and melt processes are disabled by setting $f_{si} = 0$ in (3.2). Of course arguments can be made for using B–K$_1$ as the basis of similar sensitivity experiments, but the computational resources are not available to pursue more than one option.

b. Net annual-mean heat and freshwater fluxes

The global annual-mean net heat and freshwater fluxes and individual flux components are shown in Table 2 for the original and adjusted diagnostic calculations using the Shea et al. (1990) SSTs, along with the equilibrium B–K solution. The primary balance in the global

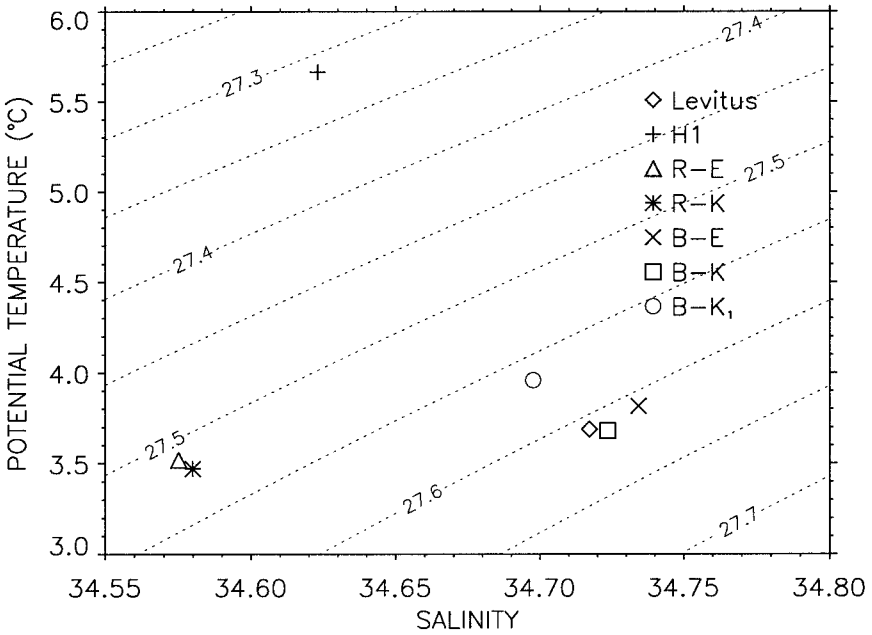

FIG. 2. Volume-averaged annual-mean potential temperature and salinity. Case H1 is from Danabasoglu and McWilliams (1995) and represents an integration with the horizontal tracer eddy diffusivity set to 1.0×10^3 m^2 s^{-1}. The climatological potential temperatures are computed from Levitus (1982) in situ temperatures. The dotted lines represent potential density (referenced to 6 m) contours in sigma units.

heat budget is between solar warming and evaporative cooling, with smaller contributions from the net longwave and sensible heat fluxes. As desired, the net heat and freshwater fluxes with the adjusted atmospheric climatology are near zero, and the global-mean θ_1 in the B–K solution (18.090°C) is nearly identical to that of the Shea et al. (1990) climatology (18.080°C).

The global, volume-average temperatures and salinities of some equilibrium solutions and the Levitus (1982) climatology are presented in Fig. 2. The displacements from climatology reflect the integrated net surface heat and freshwater imbalances as well as nonconservative effects of the acceleration technique (Danabasoglu et al. 1996). As in DM95, the combination of surface restoring and the Gent and McWilliams (1990) mesoscale eddy transport parameterization leads to global mean states of R–E and R–K that are about 0.2°C too cold and nearly 0.15 ppt too fresh (Fig. 2). Without the eddy transport of tracers (DM95, case H1), the mean state is much too warm and still too fresh (Fig. 2).

In contrast, the bulk flux forcing cases fall much closer to the Levitus (1982) averages (Fig. 2). In part, this improvement reflects the methods used for integrating to steady state, in particular the annual adjustment of the precipitation field (appendix A). However, the net freshwater flux is not constrained to be zero, so there is some drift away from the initial Levitus (1982) global average. The least drift in both θ and S occurs for B–K. Comparison with B–E shows the overall cooling and freshening improvements due to KPP. The sea ice formation appears to have a similar influence, because the B–K_2 result (not shown) is very close to B–E in Fig. 2. The stronger under-ice restoring of B-K relative to B–K_1 leads to about a 0.25°C cooling improvement and is responsible for about 15% of the salinity improvement over the restoring cases in Fig. 2.

Annual-mean temperature and salinity distributions arise from water mass formation processes, that is, from a combination of the surface property fields and net heat and freshwater fluxes (Figs. 3 and 4). The annual-mean model net heat flux maps are generally quite similar to those constructed by Oberhuber (1988) from the COADS data. There is net warming in the Tropics and eastern subtropics and cooling in the western boundary currents and high latitudes (Fig. 3). Note that the Oberhuber (1988) flux fields have been masked out in areas where the data coverage from the COADS data is too poor. Elsewhere, the overall similarity is expected because similar empirical bulk flux formulas are used. The balance in the model (e.g., B–K, Table 2) differs, however, in that the dominant terms, the net short-wave and latent heat fluxes, are both larger than those in the Oberhuber (1988) fields. Other regional differences also arise, such as 1) in the western boundary current regions (e.g., Gulf Stream, Kuroshio) where the model poleward and eastward transports of warm surface water appears to be too weak and 2) offshore of western North Africa where the model actually loses heat perhaps due to too little upwelling. Several pockets of large net annual cooling are observed in the model Southern Ocean near

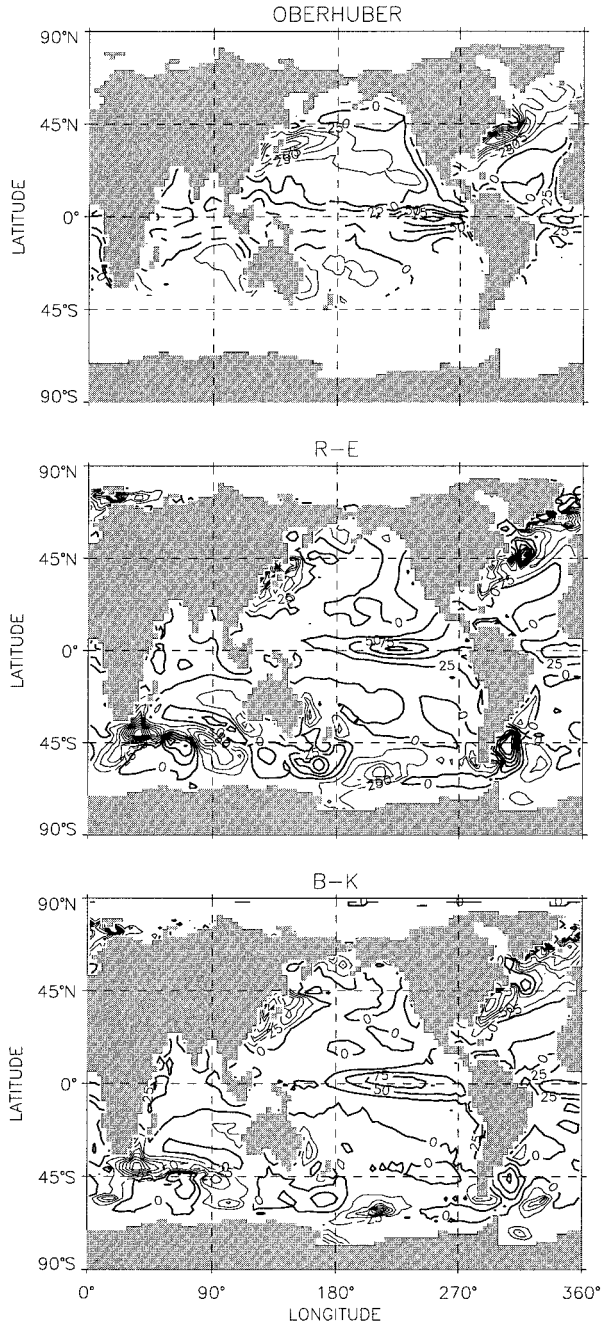

FIG. 3. Annual-mean surface net heat flux from the Oberhuber (1988) COADS climatology, and the R–E and B–K near-equilibrium solutions. The contour interval is 25 W m^{-2}. The thin lines represent negative contour levels and indicate oceanic heat loss.

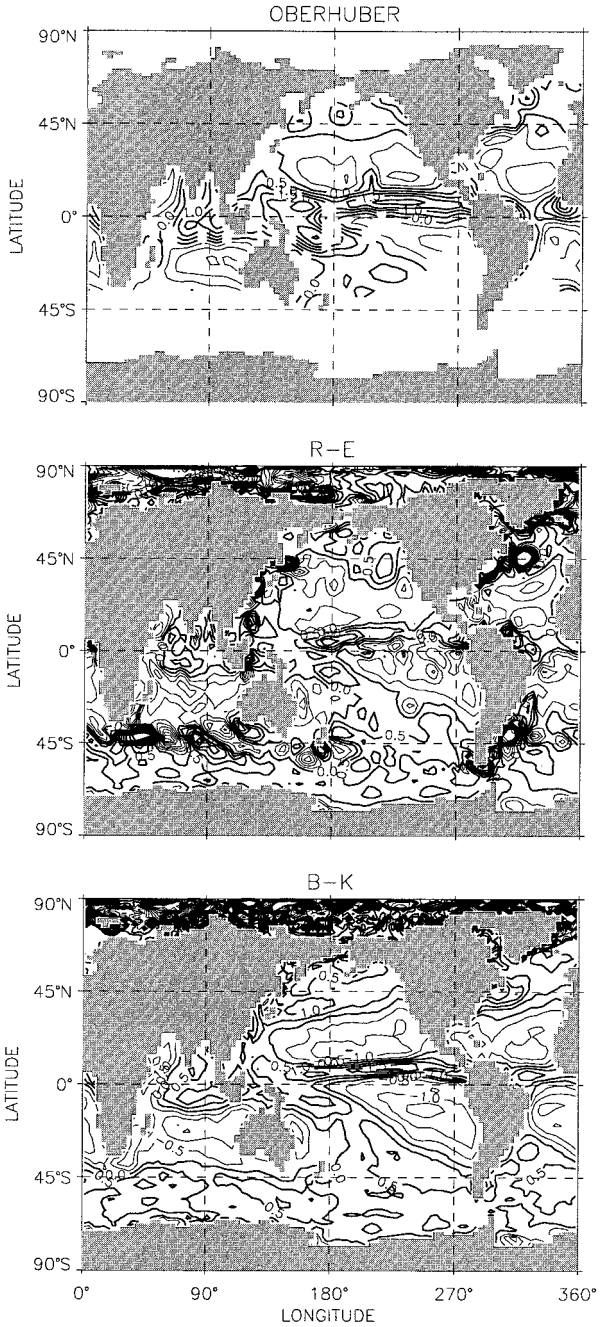

FIG. 4. Annual-mean surface net freshwater flux from the Oberhuber (1988) COADS climatology and the R–E and B–K near-equilibrium solutions. The contour interval is 0.5 m yr^{-1} (16 mg m^{-2} s^{-1}). The thin lines represent negative contour levels and indicate oceanic freshwater loss. The local maximum in R–E at 45°N, 320°E in the North Atlantic is 8.9 m yr^{-1}.

the boundary between open ocean and sea ice. The model regions of deep-water formation in the North Atlantic and Antarctic are also marked as regions of net cooling.

The net freshwater field over the ocean is less well known from observations, particularly with regards to precipitation (Schmitt 1994). Nevertheless, the overall patterns from the model are broadly consistent with the Oberhuber (1988) climatology with net freshwater input in the Tropics, high latitudes and the South Pacific convergence zone, and with net evaporation in the subtropical gyres (Fig. 4). One exception is the midlatitude storm track regions, where the satellite-based MSU data suggest higher precipitation rates. The effect of the strong under-

ice restoring in the Arctic, perhaps coupled with the Fourier filtering, is shown by the large amplitude variations in the net freshwater flux on short spatial scales. This effect is somewhat reduced by the weaker under-ice restoring of R–E and B–K_1 compared to B–K.

Although the equilibrium fluxes of R–E and B–K display similar patterns and generally agree within uncertainties with Oberhuber (1988), there are differences in detail. These differences, when accumulated over time and integrated spatially, lead to significant differences in model solutions. In addition to the global averages of Fig. 2, we shall show in section 5 that restoring and bulk forcing produce differences in basin average property profiles, meridional overturning, and poleward heat and freshwater transport.

4. Vertical mixing

The general forms of the subgrid-scale vertical mixing of horizontal momentum **u** and of any tracer τ are

$$(A_{MV}(\mathbf{u})_z)_z \quad \text{and} \quad (A_{\tau V}[(\tau)_z - \gamma_\tau])_z, \tag{4.1}$$

respectively. Here, z is the vertical coordinate, positive upward, and in subscript form it denotes partial differentiation. The KPP vertical mixing scheme is used to determine the profiles of viscosity A_{MV}, tracer diffusivity $A_{\tau V}$, and nonlocal boundary layer tracer transport γ_τ. The first step is to diagnose the depth $h_{\rm bl}$ of the oceanic boundary layer, which can be very different than the mixed layer depth. Essentially $h_{\rm bl}$ is a measure of how deep a turbulent boundary layer eddy with a near-surface velocity and buoyancy can penetrate into the interior stratification before becoming stable, in a Richardson number sense, relative to the local velocity and buoyancy. Numerically it is the shallowest depth that an appropriate Richardson number first exceeds a critical value, $\mathrm{Ri}_c = 0.3$. Further details are given in Large et al. (1994).

In KPP cases, the three vertical mixing processes active in the ocean interior below $h_{\rm bl}$ are internal wave breaking, vertical shear instability, and convection, but double diffusion is not enabled. All three are parameterized as downgradient fluxes (see Large et al. 1994 for detailed descriptions), so their local mixing coefficients are simply summed to give the profiles of effective overall interior viscosity and diffusivity. Internal wave breaking is assumed to contribute background mixing everywhere in the interior and is, therefore, parameterized by constant viscosity and diffusivity coefficients; 16.7×10^{-4} and 0.5×10^{-4} m^2 s^{-1}, respectively. As the local gradient Richardson number Ri_g decreases from 0.7 to 0.0, the mixing coefficients associated with resolved vertical shear instability increase nonlinearly from zero to 50×10^{-4} m^2 s^{-1} for both momentum and tracers. In convective regions of the ocean interior, $\mathrm{Ri}_g < 0$, these coefficients are greatly increased to 1000×10^{-4} m^2 s^{-1}.

The profile of mixing coefficients in the boundary layer ($0 < \sigma = -z/h_{\rm bl} < 1$) is expressed as the product of depth-dependent turbulent velocity scales, w_M and w_τ, and a nondimensional vertical shape function $G(\sigma)$:

$$A_{MV}(\sigma) = h_{bl} w_M(\sigma) G(\sigma),$$
$$A_{\tau V}(\sigma) = h_{bl} w_\tau(\sigma) G(\sigma). \tag{4.2}$$

At all depths the mixing coefficients are directly proportional to $h_{\rm bl}$, reflecting the ability of deeper boundary layers to contain larger, more efficient turbulent eddies. The shape function is a cubic polynomial (O'Brien 1970)

$$G(\sigma) = \sigma(1 + a_2\sigma + a_3\sigma^2). \tag{4.3}$$

The physical condition that turbulent eddies do not cross the surface is satisfied because $G(0) = 0$. It can be shown (Large et al. 1994) that in the surface layer, $\sigma < 0.1$, Monin–Obukhov similarity theory is satisfied by (4.1), (4.2), and (4.3) if the turbulent velocity scales are properly formulated. Under neutral forcing the turbulent velocity scales are proportional to the friction velocity and in pure convective forcing depend on the convective velocity scale, with a blending of the two under the usual combination of wind and buoyancy forcing. The coefficients a_2 and a_3 in (4.3) are computed to make the interior and boundary layer diffusivities and their gradients match at $\sigma = 1$; $z = -h_{\rm bl}$. Thus, interior mixing is able to influence the entire boundary layer.

The nonlocal transport term in (4.1) is nonzero only in the boundary layer for tracers under unstable (convective) forcing. In these conditions it is parameterized by Large et al. (1994) as

$$\gamma_\tau = 15.8 \frac{\overline{w\tau}(0)}{w_\tau(\sigma) h_{bl}}, \tag{4.4}$$

where $\overline{w\tau}(0)$ is the surface kinematic flux of the appropriate tracer. The surface potential temperature flux $\overline{w\theta}(0)$ includes the solar radiation absorbed within the boundary layer. For nonzero γ_τ, mixing can occur in regions with no vertical gradients, and the tracer fluxes can be countergradient. Even though there is vigorous mixing in the boundary layer, sufficient buoyancy loss through the surface can maintain local static instability, as observed by Anis and Moum (1992).

In R–E, B–E, and DM95 the vertical mixing is more conventional. There is only downgradient diffusion ($\gamma_\tau = 0$). Nearly everywhere below 50-m depth, the mixing coefficients are set at the minimum KPP interior values: $A_{MV} = 16.7 \times 10^{-4}$ and $A_{\tau V} = 0.5 \times 10^{-4}$ m^2 s^{-1}. Above 50-m depth both A_{MV} and $A_{\tau V}$ take on KPP values given by (4.2) for $h_{\rm bl} = 50$ m, $a_2 = -2$, $a_3 = 1$, and neutral forcing with a wind speed of 7 m s^{-1} ($w_M = w_\tau = 0.003$ m s^{-1}). This enhanced mixing is strong (e.g., $A_{MV} = A_{\tau V} = 200 \times 10^{-4}$ m^2 s^{-1} at 12-m depth) and effectively mixes the upper 50 m in R–E and B–E, but has no effect on DM95 whose uppermost level is 50 m thick. The exception to these rules is that anywhere there is diagnosed gravitational instability, the mixing coefficients

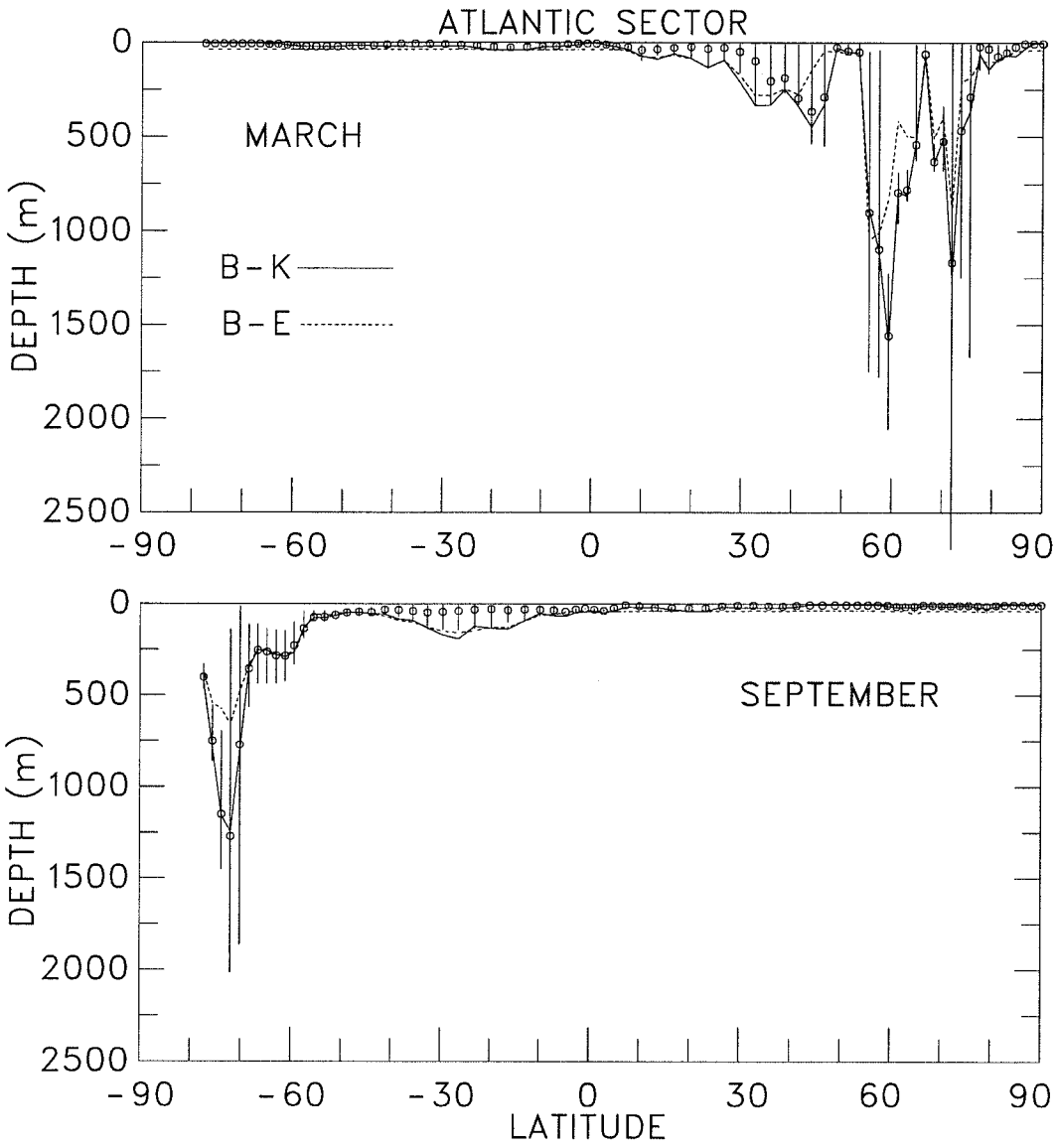

FIG. 5. March and September monthly mean mixed layer depths from B–K (solid line) and B–E (dotted line), and boundary layer depths from B–K (circles) along the 3 gridpoint wide (10.8° of longitude) meridional section of the model Atlantic Ocean shown in Fig. 1. Vertical bars extend over the range of boundary layer depths encountered in the space–time averaging.

are much larger than in KPP. Hirst and Cai (1994) report little change in model solutions for these convective coefficients in the range 1 to 1000 $m^2\ s^{-1}$, so R–E and B–E use intermediate values of $A_{MV} = A_{\tau V} = 100\ m^2\ s^{-1}$.

Figure 5 shows meridional sections of the average mixed layer depths from B–K and B–E, and the averages and ranges of h_{bl} from B–K for March and September. From among the numerous definitions of mixed layer depth, the following is adopted because it can be applied globally throughout the annual cycle. First, the discrete model profile of buoyancy b_k at depth $-z_k$ is scanned for the maximum of $(b_k - b_1)\ z_k^{-1}$, where the first level buoyancy b_1 is equated to the surface buoyancy. The mixed layer depth h_{ml} is then the shallowest depth where the local, interpolated buoyancy gradient equals this maximum. Buoyancy profiles that are linear and stable to the bottom are assigned $h_{ml} = -z_1$. Whenever all deeper buoyancies are greater than or equal to b_1, the mixed layer depth equals the depth of the bottom level.

KPP mixing develops boundary layers that are highly variable both spatially and temporally (Fig. 5). Monthly averages of h_{bl} (circles) are much shallower in the summer hemisphere than the winter. In the winter hemisphere the maximum boundary layer depth can reach the deepest model grid point, and it is often much deeper

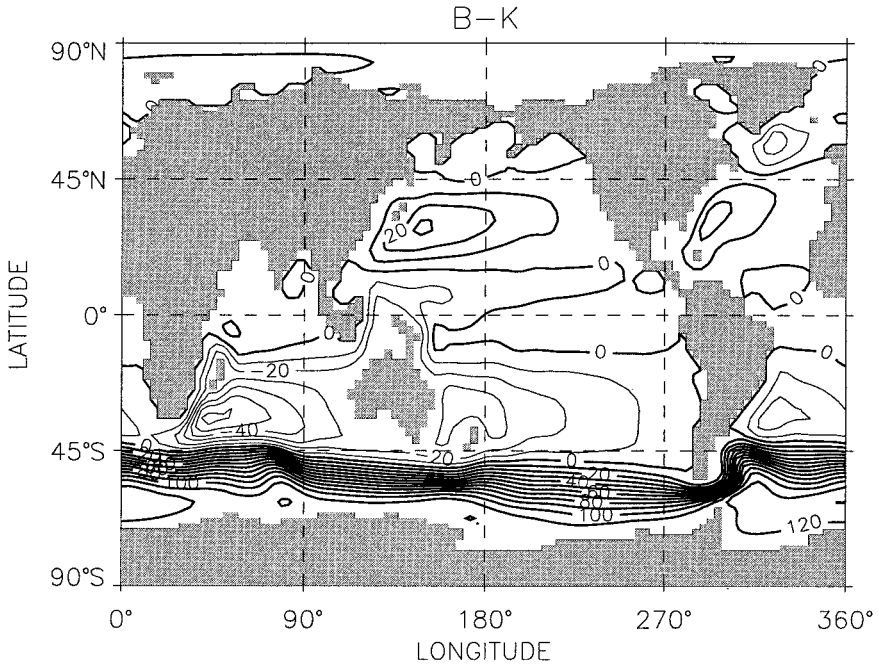

FIG. 6. Annual-mean vertically integrated mass transport (barotropic) streamfunction from B–K. Contour interval is 10 Sv. The thin lines represent negative contour levels and indicate counterclockwise circulation.

than the average of h_{bl}. This characteristic can lead to average mixed layers that are deeper than average boundary layers. In regions of known deep convection, the Weddell Sea, the Nordic Seas, and the western subpolar gyre of the North Atlantic, the boundary layer with its large mixing coefficients reaches well below the mixed layer to beyond 2000-m depth. The latter is observed in the Labrador Sea, but occurs in the Irminger Sea region in the model. This penetrative mixing parameterizes the entrainment caused by convective elements that extend throughout the boundary layer. However, the boundary layer is not at its maximum long enough for the mixed layer to reach as deep. Nonetheless, the deep mixed layers produced by KPP mixing in B–K are 200 to 700 m deeper than the convective mixed layers of B–E (Fig. 5). In these coarse-resolution models there is little anticyclonic circulation and no deep mixing in the Labrador Sea. The wintertime mixed layer depths in the subtropical gyres of B–K are about 400 m in the North Atlantic and about 200 m in the South Atlantic. The B–E depths are comparable, except around 45°N.

In the summer hemisphere and equatorial regions the convective mixing of B–E does not operate, and the mixed layer depth is uniformly pegged at 50 m by the enhanced mixing. The KPP mixing tends to produce shallower mixing and, hence, warmer surface temperatures and more sensitivity to surface fluxes. Between about 60° and 70°S there is a distinct annual cycle of mixing at all longitudes in response to the annual cycles of heating and wind stress. The latter has an average amplitude of about 0.05 N m^{-2} and is out of phase with the former (Trenberth et al. 1990). The strong winter winds and cooling produce maximum boundary layer depths of nearly 500 m and average mixed layer depths in both B–K and B–E of about 300 m. In the Indian and Pacific sectors there is another distinct band of mixing to similar depths south of 70°S, especially evident in the Ross Sea. Vertical mixing depths in the northern Indian Ocean are shallower ($<$100 m) and display a monsoon-related annual cycle.

5. Annual-mean climatology

a. Barotropic streamfunction

The vertically integrated mass transport (barotropic) streamfunction is shown in Fig. 6 only for B–K. The gyre patterns and transport magnitudes depend mainly on the wind forcing and are, because of the identical winds, very similar in all solutions. In the Northern Hemisphere, both the Atlantic and Pacific contain a cyclonic subpolar gyre, an anticyclonic subtropical gyre, and a weak cyclonic tropical gyre. An anticyclonic gyre centered north of the Bering Strait is present in the Arctic, but with a transport of only 5 Sv (Sv $\equiv 10^6$ m^3 s^{-1}) it is not revealed by the contour interval of Fig. 6. Just south of the equator there are weak cyclonic tropical gyres in all three ocean basins, with the strongest transport being 12 Sv in the Indian Ocean off the coast of Africa. The spatial patterns of the southern Indian and Atlantic subtropical gyres are rectangular and triangular,

respectively, in accord with Stramma and Lutjeharms (1997) and Peterson and Stramma (1991).

In the North Atlantic, the maximum Gulf Stream transports are 22 and 26 Sv in R–E and B–K, respectively. Even though these transports include components from both the Florida Straits and Antilles Current, they are smaller than the voltage-derived estimate of 32.2 ± 3.2 Sv for the Florida Current alone (Larsen 1992). Of course, downstream observations of the Gulf Stream that include the larger recirculation component that is missing in the model are necessarily much greater (e.g., 150 Sv, Hogg 1992). Similarly, the model Kuroshio transport is low. Weak western boundary currents are typical of coarse-resolution models and are even weaker in the coarser resolution of DM95. An obvious model problem is evident here in the 14 Sv of transport through the Sea of Japan. This flow of warm water north of Japan is primarily responsible for the surface flux differences seen in this region of Figs. 3 and 4. The model circulation between Iceland and Europe is everywhere northward and about 3 and 5 Sv in R–E and B–K, respectively. A comparable observational estimate for the Atlantic inflow into the Nordic Seas is about 8 Sv (Gould et al. 1985).

In addition to the wind forcing, the Antarctic Circumpolar Current (ACC) transport through Drake Passage depends on A_I, as demonstrated by DM95, and on bottom topography. It ranges from 117 Sv (B–K) to 122 (B–E), and is 119 Sv in R–E. Thus, there is little sensitivity to the vertical mixing, and even less to the boundary conditions of the variants. For the $A_I = 0.8 \times 10^3$ m^2 s^{-1} of these cases, we interpolate among the DM95 solutions to estimate a comparable transport of about 140 Sv. We believe the greater DM95 transport is due primarily to the deeper and wider Drake Passage and secondarily to the somewhat stronger winds. The ACC transport has not been tightly constrained by observations, with the Whitworth (1983) estimate of 118 to 146 Sv being consistent with all the above values.

The Indonesian Throughflow is 22 and 24 Sv in R–E and B–K, respectively, and 19 Sv for Case I1 in DM95. Although these are consistent with the Fieux et al. (1994) observational estimate of 18.6 ± 7 Sv, they tend to be larger than most estimates (e.g., Godfrey 1989). In some preliminary integrations not reported here the smaller transport in DM95 appears to be related to the greater Drake Passage width and transport. We compute the maximum Agulhas Current transport as 66 and 70 Sv in R–E and B–K, respectively. Although these transports agree very well with the observational estimates of Stramma and Lutjeharms (1997), the model Mozambique Channel transport of 25 Sv is significantly larger than their observational estimate of 5 Sv. In all cases, the maximum Brazil Current transport is about 30 Sv, which is on the high side of most upper-level observational estimates (e.g., Peterson and Stramma 1991).

b. Potential temperature and salinity distributions

The vertical distributions of the horizontal-mean θ are shown in Fig. 7 for both the entire globe and individual ocean basins, while estimates of the uncertainties associated with not reaching absolute equilibrium are given in Table 1. In addition, Table 3 gives the root-mean-square differences from Levitus (1982). For such purposes, the southern basin includes all ocean south of 33°S plus the Great Australian Bight. The Arctic is all ocean north of the Arctic circle excluding Baffin Bay, which is part of the Atlantic, and all of the Indonesian Channel south of the equator is part of the Indian basin. The characteristics of the vertical profiles are very similar in each basin, with the exception of the Arctic. Therefore, the global average is, in general, representative of the individual basins. Deep, global averages are below 0°C in and R–E and R–K, but not in B–E, B–K, B–K_1, and DM95. Thus, the upgraded topography and resolution increases the cold bias, but the bulk forcing more than compensates, such that deep temperatures are nearer Levitus in the bulk forcing solutions (e.g., B–K; Fig. 7). There is a corresponding reduction in the rms differences in deep θ, which is sufficient to dominate the whole ocean volume (Table 3). However, the stronger under-ice restoring of B–K degrades deep θ relative to B–K_1 both in the mean (by almost 0.5°C; section 6) and in the rms difference (0.52° to 0.81°C; Table 3). At middepths (903–2510 m) the colder B–K temperatures relative to B–K_1 represent an improvement that is reflected in a smaller rms difference of 0.65°C.

The vertical temperature gradients of B–K are as steep, or steeper, than those of Levitus throughout most of the water column, except above about 400-m depth. In the Arctic, there is a realistic temperature inversion in the upper 400 m, but deeper there is a warm bias. The B–K Atlantic has the most distinctive differences from Levitus, and these persist in all bulk forcing variants. In particular, the warm bias extends deeper than in the global to 2200 m, and at 3000 m the stronger vertical gradient leads to a much colder bias than seen in the other basins. These features are indicative of too shallow penetration of warm North Atlantic Deep Water (NADW) being compensated by too much cold Antarctic Bottom Water (AABW).

The zonal-mean potential temperature distributions are presented in Fig. 8 in comparison to the Levitus (1982) climatology. The difference patterns and magnitudes are very similar in both R–E and B–K. The upper-ocean warm bias of Fig. 7 is evident at most latitudes, but is strongest within 45° of the equator. The large warm bias near the equator is a common feature of coarse-resolution models and it is related to weak zonal currents and weak zonal slopes of the isotherms. The model maintains the observed vertical θ gradients (vertical contours in the difference plots of Fig. 8) to 1000-m depth in the vicinity of both 45°S and 30°N. The dominant features of the vertical gradients seen in

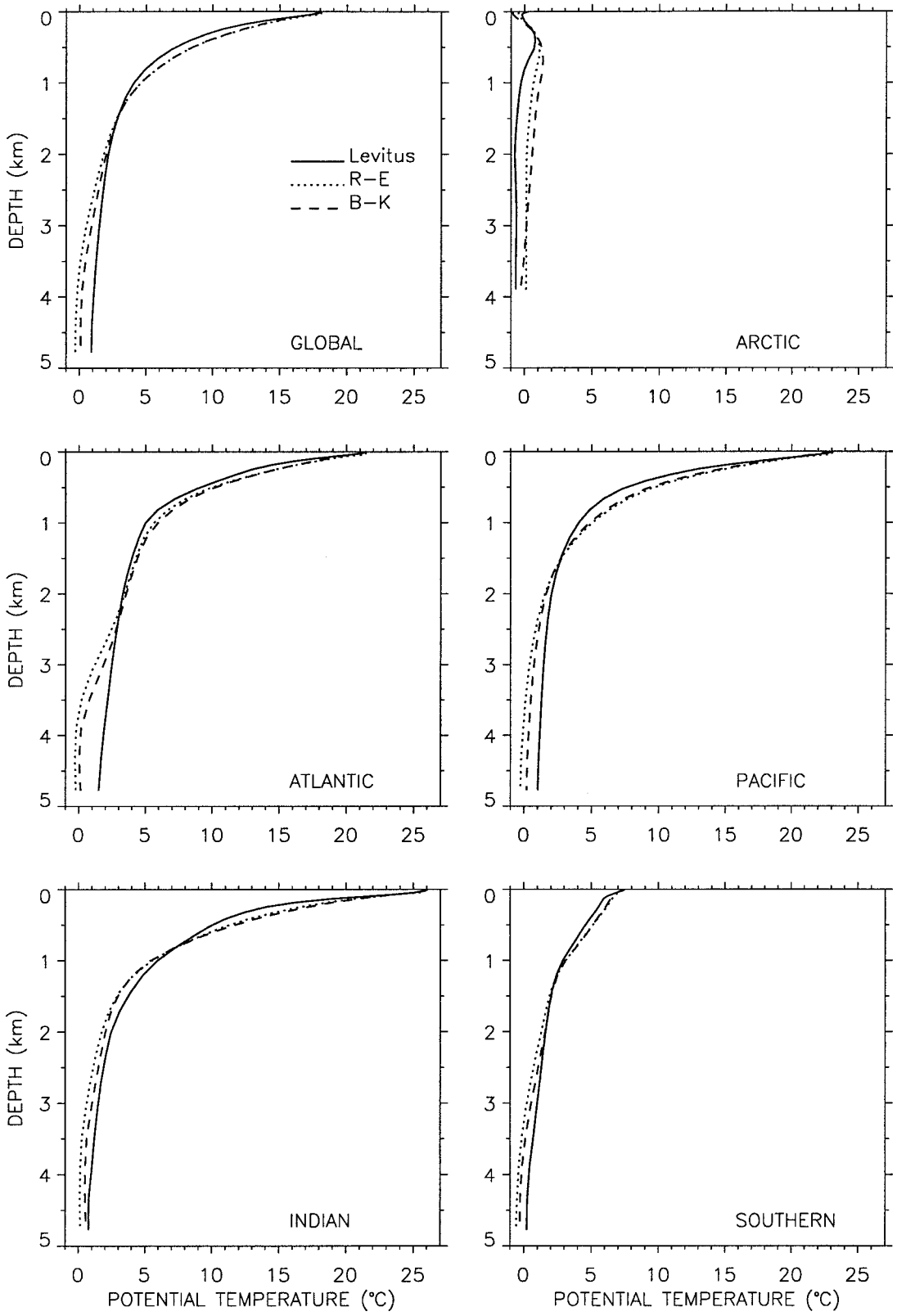

FIG. 7. Vertical profiles of the annual- and horizontal-mean potential temperature.

TABLE 3. Model experiments—Levitus (1982) climatology rms differences in θ and S. In addition to the entire ocean volume values, the difference rms is computed separately between depth intervals of 0–903 m, 903–2510 m, and 2510–5000 m as representatives of the upper, middepth, and abyssal ocean solutions, respectively; θ and S are in degrees Celsius and parts per thousand.

	0–903 m		903–2510 m		2510–5000 m		0–5000 m	
	θ	S	θ	S	θ	S	θ	S
R–E	1.89	0.24	0.71	0.17	1.16	0.21	1.24	0.20
R–K	1.81	0.23	0.71	0.17	1.17	0.21	1.22	0.20
B–K_1	1.92	0.28	0.73	0.11	0.52	0.09	1.09	0.16
B–K	1.89	0.28	0.65	0.10	0.81	0.05	1.12	0.16
B–K_2	1.96	0.29	0.67	0.11	0.70	0.05	1.13	0.16
B–E	1.98	0.30	0.63	0.11	0.74	0.06	1.14	0.16

Fig. 7 are mostly confined to between these latitudes. All three solutions (Figs. 8b, 8c, and 8d) have a large error pattern at about 65°N due to a false poleward displacement of the sub-Arctic Front. However, this displacement and the magnitude of this error are substantially less than in DM95 because of the more realistic Icelandic Ridge topography. In the abyssal ocean, the cold bias displayed by the solutions is present at all latitudes but is about 0.5°C less in B–K than in R–E. This improvement is not due to the use of KPP, as shown by the similarity between B–K (Fig. 8c) and B–E (Fig. 8d). Nor should it be attributed to the larger under-ice restoring coefficients, because this bias is even smaller in B–K_1, as discussed in section 6, than in B–K. Therefore, the use of open-ocean bulk forcing appears to markedly improve the deep cold bias of the restoring cases. DM95 showed that the bias is also sensitive to the isopycnal transport parameterization.

The near-surface temperatures of Fig. 8b show the effectiveness of restoring at keeping model temperatures near observed. However, this control does not penetrate much beyond the uppermost level. With bulk forcing, the B–K and B–E surface temperatures are somewhat cooler than the Levitus (1982) climatology, especially in the Northern Hemisphere, but the rms differences in R–E and B–K are the same (Table 3). The effect of KPP mixing can be seen by comparing Figs. 8c and 8d. There is a distinct improvement in temperatures above about 200 m, north of 40°S. Farther south both solutions are very similar at these depths and are within ± 0.5°C of Levitus (1982) nearly everywhere. The vertical extension of surface control by KPP mixing is suggested also by the smaller rms differences in R–K and B–K compared to R–E and B–E, respectively, over the upper 903 m (Table 3).

The improvements with B–K are more striking in the vertical distributions of the horizontal-mean S (Fig. 9). Because surface salinity is strongly restored to the climatology, the near surface S for R–E tends to be closer to the observations than for B–K. In spite of this constraint, R–E cannot maintain the observed upper-ocean vertical S gradients, except in the Atlantic. With this exception, R–E profiles are consistently fresher than the observations at all depths, typically by about 0.2 ppt below 2000 m. The global average profiles of R–E and of R–K are very much alike. They are fresher than Levitus all depths, with most of the 0.14 ppt fresh bias of Fig. 2 coming from below about 1500 m. This bias is accompanied by large rms S differences in R–E and R–K that dominate the whole ocean volume (Table 3). It is largely found in the Atlantic where the salinity profile becomes fresher by more than 0.3 ppt below 3000 m.

In B–K, the near-surface salinity follows the observational values more closely than R–E only in the Arctic where there is strong under-ice restoring, and in the Indian Ocean. Hence, the somewhat larger rms S differences in the upper 903 m (Table 3). The upper-ocean vertical S gradients of B–K are in good agreement with the climatological gradients in all basins, indicating a well-simulated halocline. The depth of the subsurface S maximum also agrees well with the observations in all basins. The Arctic, Pacific, Indian, and Southern Ocean profiles below 1000 m follow the Levitus (1982) profile very closely: slightly more saline between about 1000–3000 m and slightly fresher farther down. This agreement is reflected also in the rms S differences (Table 3). These values are much reduced below 2510-m depth and somewhat smaller at middepths in the bulk forcing cases compared to R–E and R–K. There are similar, but smaller, B–K improvements relative to B–K_1 in both the mean (section 6) and the rms differences (Table 3), showing the sensitivity to the under-ice restoring.

The missing Red Sea outflow is evident in the Indian Ocean profile of Fig. 9, as a fresh bias at about 1000 m. The largest deviations between B–K and climatology occur, like temperature, in the Atlantic, with more than a 0.1 ppt fresh bias in the abyssal ocean. This bias is about 0.2 ppt in B–K_1 (section 6). Again the Atlantic salinity profile is indicative of too shallow penetration of salty NADW being compensated by fresh AABW. Although the salinity profiles are most sensitive to boundary conditions, KPP vertical mixing leads to less of a salty bias below 1500-m depth, primarily in the Pacific, compared to B–E. This reduced salt leads to the improved average salinity in Fig. 2, but little change in rms S differences (Table 3).

Figure 10 shows the zonal-mean salinity distributions in comparison to the climatology (Levitus 1982). The most significant improvement in B–K (Fig. 10c) is that the overall fresh bias observed in R–E (Fig. 10b) is substantially eliminated, especially below 400 m. This change is almost entirely due to the bulk forcing; B–E (Fig. 10d) and R–K (not shown) salinity distributions are very similar to B–K and R–E, respectively. However, the degree of improvement is sensitive to the under-ice restoring strength and is about 30% less in B–K_1 (section 6). Nonetheless, in all bulk cases the sinking branch of the thermohaline circulation of the North Atlantic is more saline than Levitus (1982) and the restoring cases, and dilution with fresher

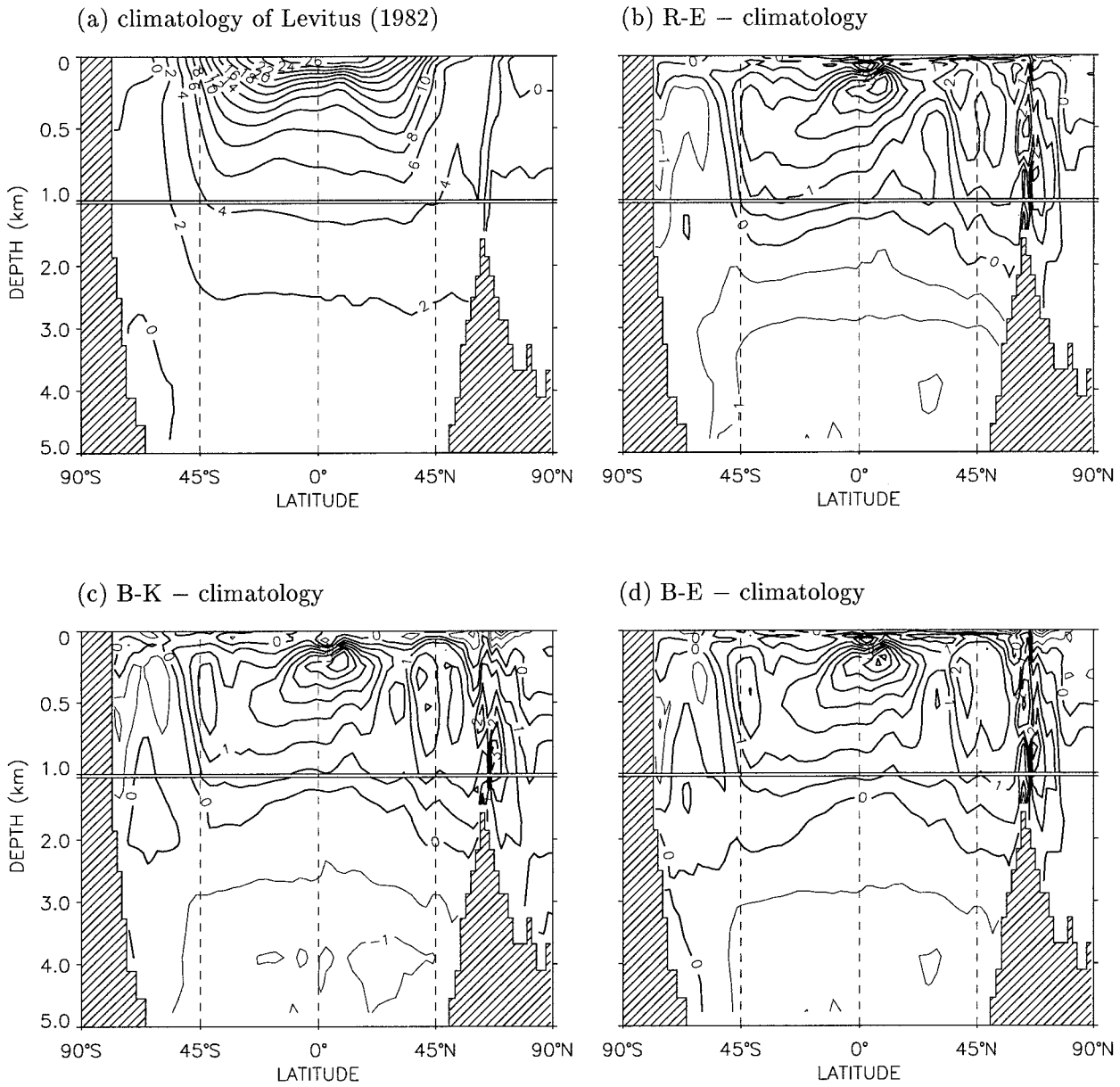

FIG. 8. Annual- and zonal-mean, global potential temperature. Contour interval is 2°C in (a) and 0.5°C in (b), (c), and (d). The thin lines represent negative contour levels.

water during the spread throughout the global ocean results in the agreement with Levitus (1982). The B–K Atlantic profiles of Fig. 9 and various subregional Atlantic profiles (not shown) are consistent with sinking of salty NADW and suggest that the dilution is with deeper, fresher AABW. A similar transformation appears in the R–E case, but the sinking water has near Levitus salinity (Figs. 9 and 10b), so the subsequent dilution results in the fresh bias observed at all depths in the restoring cases. This bias is also present in DM95, where S was similarly restored to the climatology.

What is the source of the more saline water in B–K? A likely candidate is the surface around 45°N in the western North Atlantic. The restoring in R–E keeps the surface salinity close to Levitus (1982) by producing far too much freshwater flux in this region (up to 8.9 m yr^{-1}; Fig. 4). In contrast, the more realistic (compared to Oberhuber 1988, Fig. 4) bulk forcing allows a 0.7 ppt more saline Atlantic zonal average, which is not evident in the global differences of Fig. 10c. This surface water appears to contribute to the salty NADW, which eventually relieves the deep fresh bias.

A tongue of low salinity Antarctic Intermediate Water (AAIW) is evident in the Levitus (1982) climatology (Fig. 10a) from the surface to about 1200-m depth between about 25° and 60°S. This water mass is not well repre-

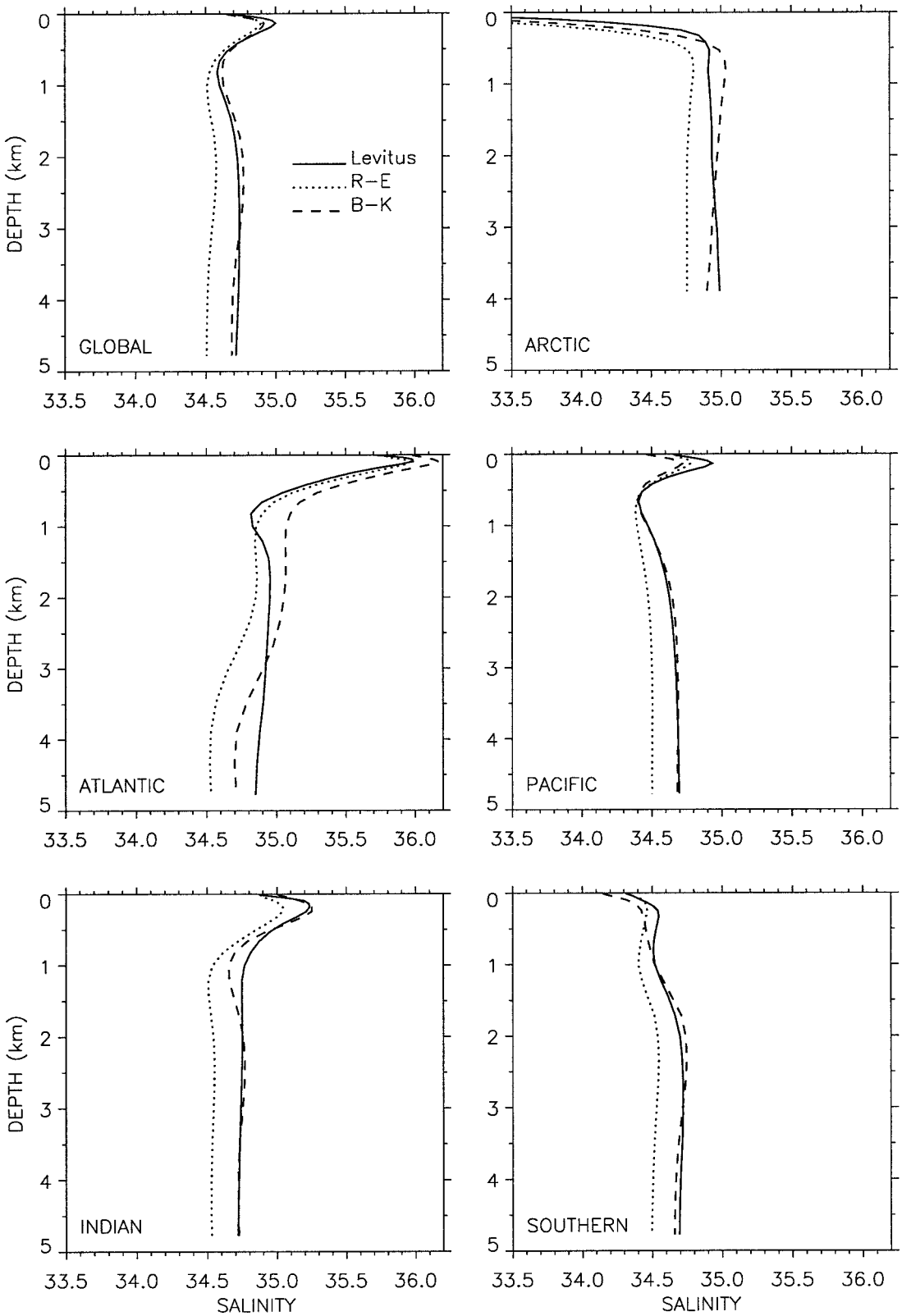

FIG. 9. Vertical profiles of the annual- and horizontal-mean salinity. In the Arctic, the first model level (6 m) salinity values are 31.63, 32.03, and 31.93 for Levitus (1982), R–E, and B–K, respectively.

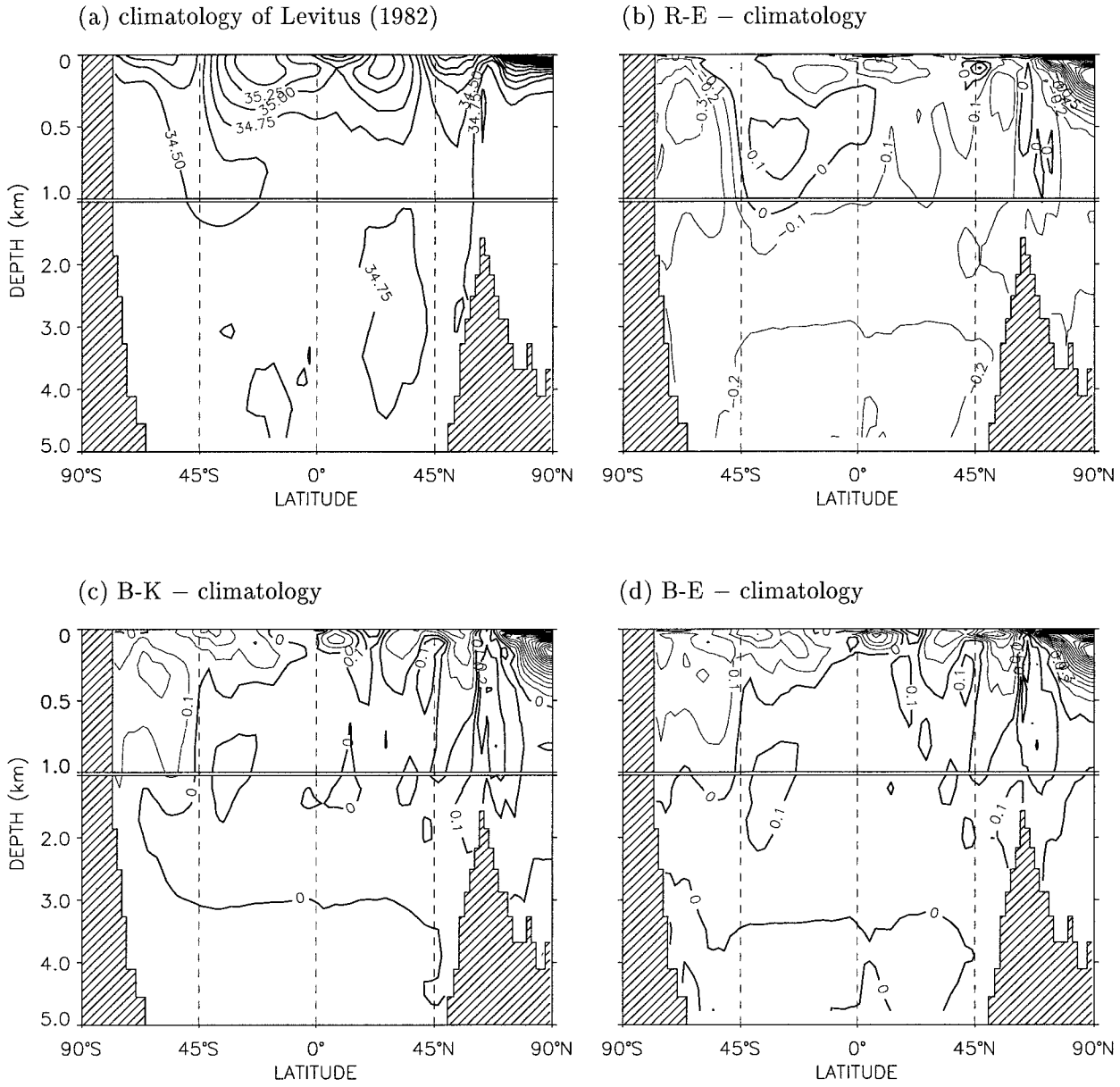

FIG. 10. Annual- and zonal-mean, global salinity. Contour interval is 0.25 in (a) and 0.1 in (b), (c), and (d). The thin lines represent negative contour levels.

sented in R–E. The salinity contrast is too weak and the penetration to shallow, which leads to the −0.2 to 0.1 ppt error pattern in Fig. 10b. There is a marked improvement in B–K (Fig. 10c), as indicated by the general 0.1 ppt reduction in the differences from Levitus (1982). The similarities in this region between B–K and B–E (Fig. 10d) demonstrates that the improved AAIW is due largely to the bulk forcing. Furthermore, it is the air–sea fluxes that are responsible. The improvement is not sensitive to the under-ice restoring because the regional differences between B–K and B–K_1 salinities are less than 0.02 ppt.

As with temperature, restoring is unable to keep the salinity near Levitus much below the 50 m of enhanced mixing. This lack of success is particularly evident in the upper Arctic where restoring is applied in all cases, and it makes a strong argument for a coupled sea ice model. Near-surface salinity in the bulk cases is much too fresh on average at nearly all latitudes. However, KPP mixing has a positive impact by overall reducing the negative bias above about 150 m in the Northern Hemisphere (compare Figs. 10c and 10d).

c. Meridional overturning streamfunction

The zonally integrated meridional overturning streamfunction distributions are presented in Fig. 11.

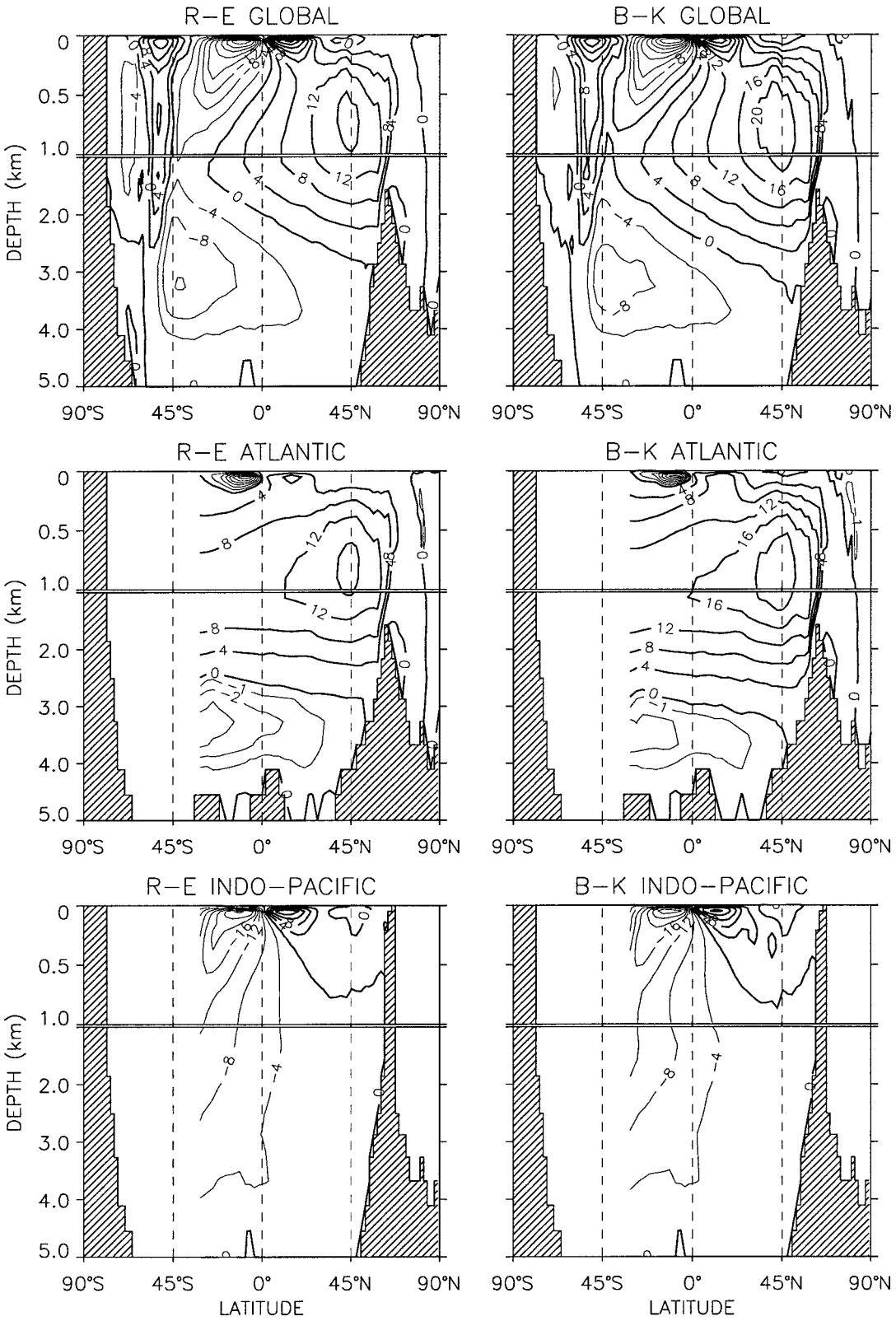

FIG. 11. Annual-mean zonally integrated meridional overturning streamfunction obtained with the effective transport velocity. Contour interval is 4 Sv except for the Atlantic where a 1-Sv interval is used for negative levels. The thin lines represent negative contour levels and indicate counterclockwise circulation.

This transport indicates the strength of the thermohaline circulation except in the upper ocean, where Ekman transport driven by the surface wind stress is dominant. For these calculations the effective transport velocity is used. This velocity is the vector sum of the Eulerian-mean velocity and the eddy-induced velocity that arises from the Gent and McWilliams (1990) isopycnal transport parameterization.

The global patterns show two shallow cells that upwell at the equator. These circulations are similar in all cases, including DM95, because they are driven by the divergence of the Ekman transport due to the easterly trade winds. Most of this upwelling occurs in the Pacific basin because of the great width. The southern cell penetrates deeper than the northern one. Overall, the Indo–Pacific meridional overturning is similar in all cases, with weak, broad upwelling in much of the basin below 1000 m. The global cell located at about 50°S is a remnant of the Eulerian-mean Deacon cell (Bryan 1991), whose mean transport is over 20 Sv at 1000-m depth (not shown). The substantial reduction in Fig 11 is due to a cancelation between mean advection and eddy-induced transport (DM95). This cancelation is not as complete in either R–E or B–K as it is in DM95, probably because of the different surface buoyancy forcing, topography, and tapering of A_I and A_{ITD} (see Gent and McWilliams 1996 for a discussion of the dynamics of this partial cancelation). The upper-ocean wind-driven circulations have a few Sv more transport in B–K than in R–E. In contrast, the circulation poleward of the Deacon cell is slightly stronger in R–E, indicating more deep-water formation there.

In the abyssal Atlantic Ocean of B–K, the AABW transports nearly 2 Sv into the Northern Hemisphere, and the associated return flow occurs between 2800 and 3500 m. This transport is slightly higher in R–E and slightly smaller in the base case of DM95.

The Northern Hemisphere meridional circulation is dominated by the thermohaline circulation, which occurs primarily in the North Atlantic. The southward branch of this circulation represents the flow of the NADW. One estimate for its transport at 24°N is about 17 ± 4 Sv (Roemmich and Wunsch 1985), which agrees very well with 18 Sv in B–K, but not quite so well with the 14 Sv of R–E. In both B–K and R–E, most of the NADW crosses the equator, with only about 7 Sv upwelling in the Northern Hemisphere. The sinking of NADW is confined to the vicinity of the Icelandic Ridge (Denmark Strait and Faroe–Shetland Channel), with what appears to be too little Nordic Sea component. With the deeper ridge topography (2500 m) of DM95, this sinking occurs about 10° farther north. We compute the maximum strengths of the thermohaline circulation as 17 and 23 Sv in R–E and B–K, respectively. The variants R–K and B–E have 17.5 and 22.5 Sv, respectively, for this transport, therefore nearly all the increase in the circulation strength is due to the bulk surface buoyancy forcing. A comparison of the R–E distribution

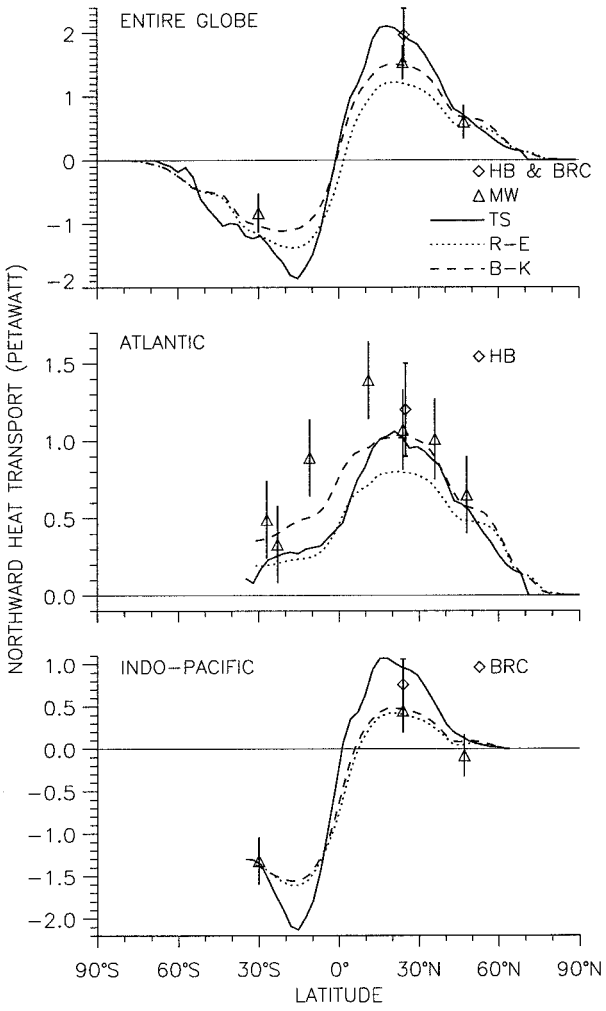

FIG. 12. Annual-mean northward heat transport. Line TS is from Trenberth and Solomon (1994), where one standard error is about ±0.4 and ±0.1 PW in low and high latitudes, respectively. MW data points (triangles with error bars) are from Macdonald and Wunsch (1996). HB and BRC data points (diamonds with error bars) are from Hall and Bryden (1982) and Bryden et al. (1991), respectively. In the global panel, the HB & BRC data point represents the sum of HB and BRC data points of the Atlantic and Indo–Pacific panels.

to case I1 of DM95 shows a slight weakening of the thermohaline circulation. This is partially due to the ridge topography, but is insensitive to the presence of Iceland as an island. Although the NADW penetration is slightly deeper (by about 200 m) in B–K, it is still not as deep as observed and the northward flowing AABW is found too shallow at about 3500 m and penetrates too far to the north.

d. Heat and freshwater transports

The annual-mean northward heat and freshwater transports are shown in Fig. 12 and Fig. 13, respectively, for the entire globe, the Atlantic, and the combined Indo–Pacific basins for both R–E and B–K. In equilib-

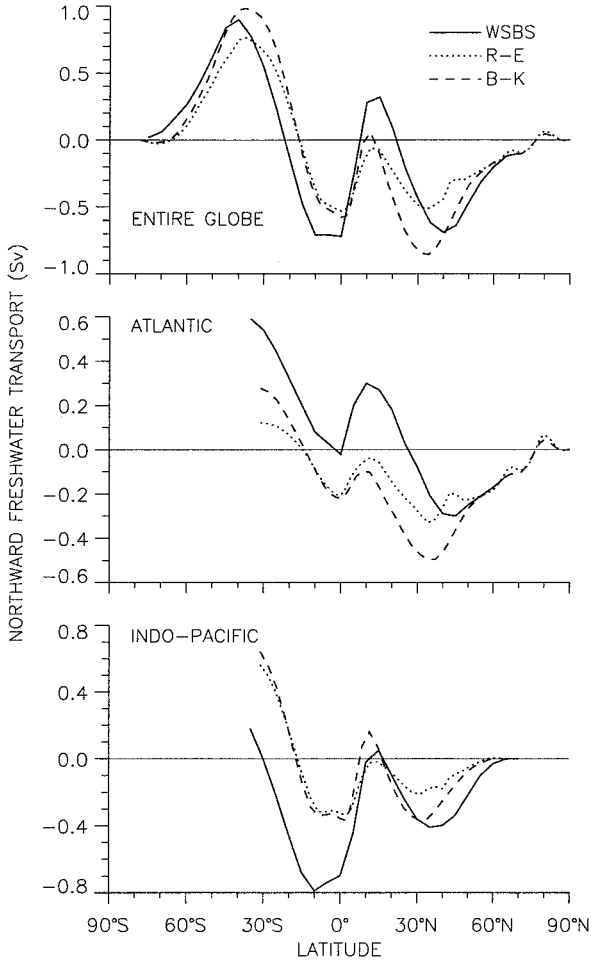

FIG. 13. Annual-mean northward freshwater transport. Line WSBS is from Wijffels et al. (1992). In the Atlantic and Indo–Pacific, lines WSBS are offset by 0.79 Sv to compensate for the missing transport through the Bering Strait in the models.

rium, the meridional derivatives are equivalent to the zonal integrals of the surface fluxes (Figs. 3 and 4). Unfortunately neither transport is tightly constrained by observation. Also shown for comparison in Fig. 12 are the residual estimates from atmospheric analyses of Trenberth and Solomon (1994), some direct observational estimates (Hall and Bryden 1982; Bryden et al. 1991), and the inverse ocean modeling results of Macdonald and Wunsch (1996). In the latter the North Brazil Current constraint at 11°N is highly variable and poorly known. A large uncertainty in the Macdonald and Wunsch (1996) transport at this latitude is consistent with the large difference from the equilibrium model results and the following calculation. A decrease in the Atlantic transport from 1.4 PW at 11°N to 1.08 PW at 24°N, implies an average surface cooling of 40 W m^{-2} over these latitudes. However, heat flux climatologies as well as the model fluxes (Fig. 3) indicate net heating, though not so much as Trenberth and Solomon (1994).

The maximum northward global transport is about 1.25 PW at 21.5°N in R–E, R–K, and DM95 and about 1.53 PW in B–K and B–E. The principal contribution to this transport occurs in the Atlantic Ocean where the change in Icelandic Ridge topography reduces the maximum from 0.90 PW in DM95 to 0.80 PW in R–E and R–K. The change in boundary conditions more than compensates by increasing this maximum more than 25%, to 1.04 PW in B–K and B–E. Consequently, the maximum Atlantic heat transports for these cases are within the estimates of 1.2 ± 0.3 PW at 25°N by Hall and Bryden (1982), 1.21 ± 0.34 PW at 26.5°N by Molinari et al. (1990), and 1.07 ± 0.26 at 24°N by Macdonald and Wunsch (1996). In DM95 the transport north of the excessively deep Icelandic Ridge is systematically larger (e.g., 0.25 PW at 70°N) than B–K because of the northward penetration of the shallow thermohaline circulation. In the Atlantic between 15°N and 11°S, the B–K heat transport systematically diverges from Trenberth and Solomon (1994), but is more consistent with the inverse estimates, especially the more reliable ones at 23° and 27°S.

Both the R–E and B–K equilibrium solutions produce Indo–Pacific heat transports that are consistent with all three Macdonald and Wunsch (1996) inverse results, but only B–K is within the uncertainty given for the Bryden et al. (1991) estimate. The maximum northward transports are 0.42 and 0.50 PW at 21°N in R–E and B–K, respectively. Both solutions indicate ocean heating at 47°N, but not enough to give the southward heat transport of the inverse calculation and the Moisan and Niiler (1997, hereafter MN) estimates. The Trenberth and Solomon (1994) residual transports indicate net ocean cooling at all latitudes north of 15°N, such that at 26°N they are more than twice the B–K values, inconsistent with both the inverse and the MN results, but just within the upper limit of Bryden et al. (1991). The discrepancies continue farther south, but these tend to cancel so that at 30°S there is agreement between all the Indo–Pacific heat transport estimates in Fig. 12.

Although the Indo–Pacific basin is the primary contributor to the global poleward heat transport in the Southern Hemisphere, the reduction in B–K relative to R–E comes mostly from the Atlantic basin. This is due to the increased flow of the NADW into the Southern Hemisphere and the associated increase of the warm, northward return flow in the upper ocean. In terms of surface heat fluxes (Fig. 3), the larger R–E transport gradient between about 40° and 20°S indicates more heat loss from the ocean.

Figure 13 shows the Wijffels et al. (1992) northward freshwater transport as found by integrating the Baumgartner and Reichel (1975) surface freshwater flux climatology and removing the Bering Strait transport of 0.79 Sv. Since this climatology extrapolates from island or land stations into remote areas of unsampled ocean, the uncertainties are large, especially in the Southern Hemisphere, but remain unquantified. The model results are very uncertain also, as reflected in the adjustments

to the bulk humidity and precipitation required to balance the global freshwater flux (appendix A). Nevertheless, in the Atlantic Ocean north of 50°N, the B–K and R–E distributions are in good agreement with the Wijffels et al. (1992) estimates.

However, in the storm track zone between 30° and 45°N there is great divergence. The large amounts of precipitation in the bulk surface forcing results in a very much larger southward transport across 33°N in B–K. This precipitation is in accord with the freshwater flux computed by Bryan and Oort (1984) from aerological data. They estimate the zonal average oceanic flux between 30° and 40°N to be 6.0 mg m^{-2} s^{-1} (0.19 m yr^{-1}), whereas Baumgartner and Reichel (1975) give −16 mg m^{-2} s^{-1} (−0.51 m yr^{-1}). Such a large difference even as to the sign of the flux attests to the very large uncertainties in freshwater flux estimates and derived transports, even in relatively well-traveled latitudes. The R–E freshwater transport and surface flux (Fig. 4) are like neither B–K nor the observational estimates in the North Atlantic storm track. The resulting biases relative to Wijffels et al. (1992) are somewhat enhanced in the subtropics, and partially compensated by too little model freshwater flux in the region of the Atlantic intertropical convergence zone from the equator to 10°N. Throughout the South Atlantic the slopes of the B–K and estimated transports generally match, implying similar net surface freshwater fluxes, but the R–E results diverge south of 15°S.

A similar pattern of agreement and difference is found in the Indo–Pacific, with two major exceptions. First, Wijffels et al. (1992) suggest much more freshwater input north of 50°N than any of the model variants. Second, they show considerable freshwater input between the equator and 10°S where the model fluxes are near zero. This difference compensates for the Atlantic difference north of the equator, so the model transports are more like Wijffels et al. (1992) in the global mean than they are in the individual basins.

In the Southern Ocean (south of 33°S in the global distributions), the major disagreement between the model solutions and observations occurs south of 70°S. Here, the model freshwater transports indicate evaporation, resulting from strong under-ice evaporative restoring of salinity in the Weddell and Ross Seas (Fig. 4). Farther north in the Southern Ocean, the B–K precipitation is somewhat larger than the observations, but neither may represent reality.

e. Equatorial and surface circulation

Even though the finest model resolution (1.8° in latitude) is at the equator, the details of the equatorial current structure are not well represented in any of the model variants. For example, there is no evidence of eastward North Equatorial Countercurrents at any depth. Nonetheless, some known features of equatorial circulation can be identified in the model solutions, but in general these tend to be weaker than observed. Figure 14 shows a Pacific Ocean section of zonal velocity averaged between 4.85°S and 4.85°N. The Equatorial Undercurrent (EUC) is seen as eastward flow at depth, whose core rises from around 200 m at 180° to about 100 m at 270°E. This slope is linked to a similar rise in the thermocline, within which the 20°C isotherm (averaged from 4.85°S to 4.85°N) rises from more than 170 m to about 50 m over these longitudes. Although this slope is similar to that observed, this isotherm tends to be about 20 m deeper than observed, because of the more diffuse model thermoclines. Other realistic characteristics of the model EUC are the location of its maximum speed at 225°E, eastward velocity down to the vicinity of 300-m depth, and the transition to westward flow between 50-m and 100-m depth.

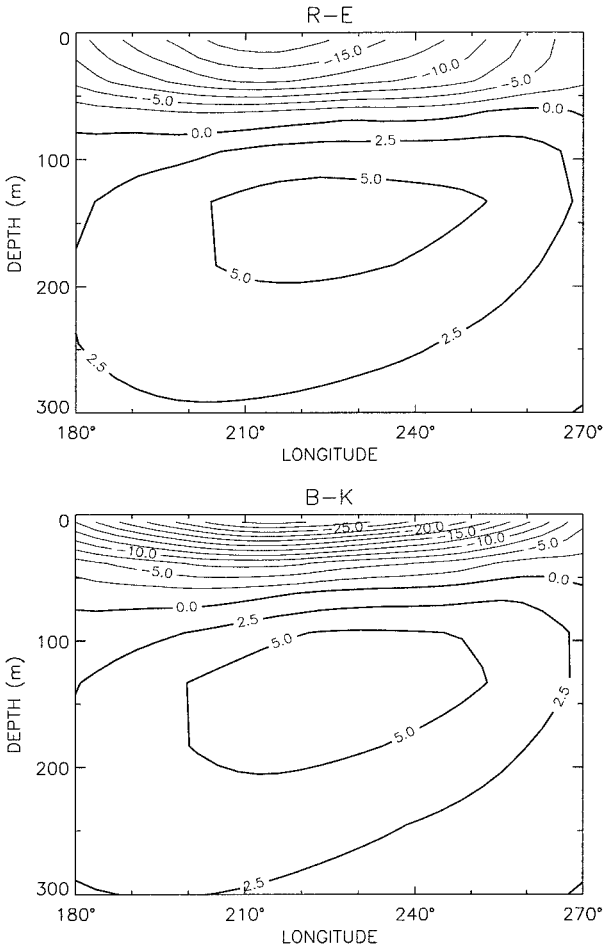

FIG. 14. Meridionally averaged zonal velocity in the equatorial Pacific. The average is computed for the region between 4.85°S and 4.85°N. The thick and thin contours indicate eastward and westward flows, respectively. The contour interval is 2.5 cm s^{-1}.

The model resolution and the related large horizontal viscosity A_{MH} causes the EUC to be much wider (10° versus 4° in latitude) than observed, and its core speed to be reduced by more than an order of magnitude.

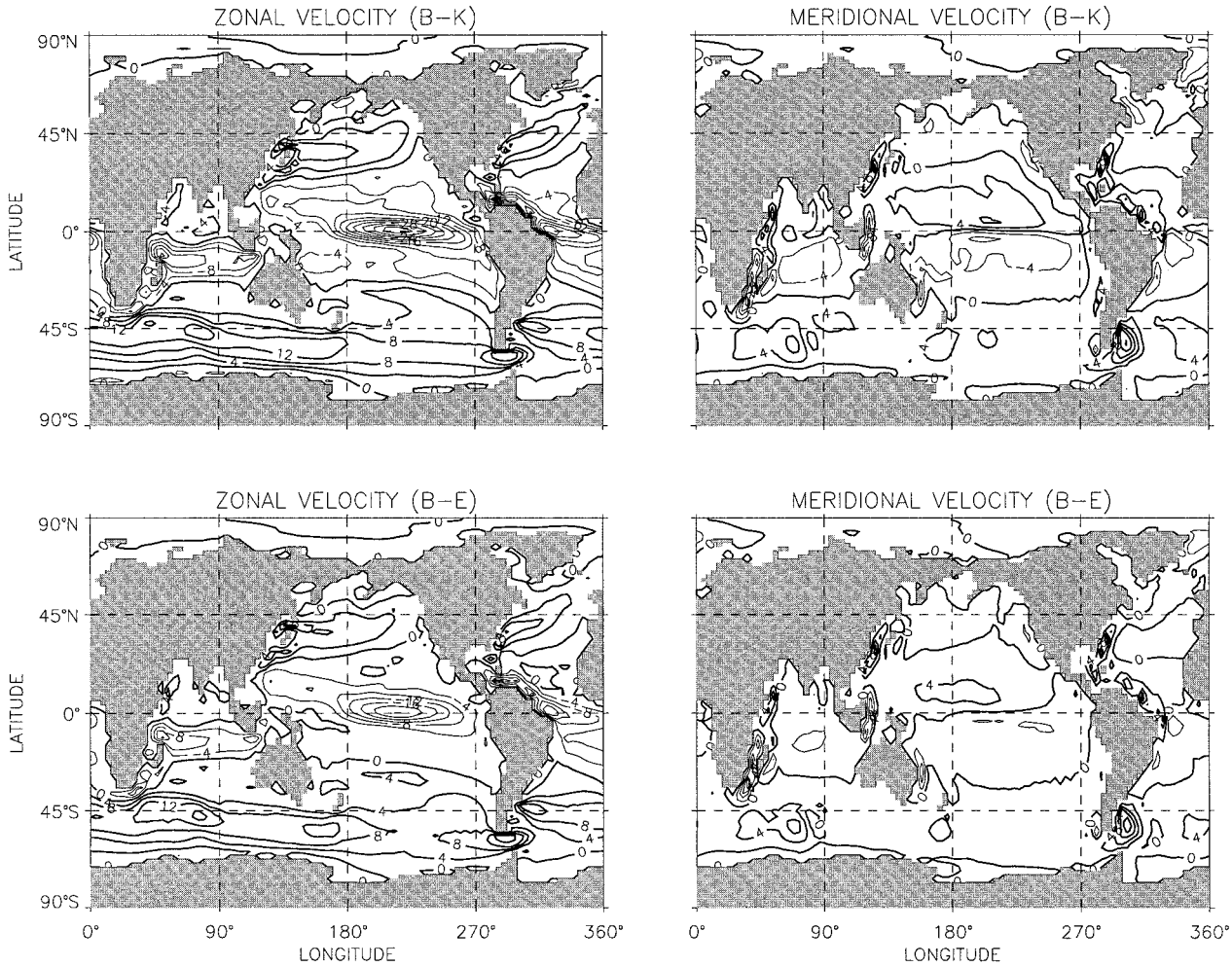

FIG. 15. Annual-mean zonal and meridional components of model upper-level (surface) velocity. In all panels the contour interval is 4 cm s^{-1}. The thick and thin contours indicate eastward or northward, and westward or southward flows, respectively.

Despite its larger cross-sectional area the reduced overall speed results in an annual-mean transport of the eastward flow of only about half the 23 Sv estimate of Wyrtki and Kilonsky (1984) for the EUC. Averaged from 180° to 270°E, this model transport between 7.2°S and 7.2°N and above 300 m is only 9.9 Sv in the equilibrium B–K solution. It is nearly 10% less in R–E, primarily because of the different subgrid-scale vertical mixing.

Another impact of KPP is that it allows for more vertical shear in the westward flowing South Equatorial Current (SEC). As a result the upper-layer velocity in Fig. 14 has a maximum of 30 cm s^{-1} in B–K, compared to less than 20 cm s^{-1} in R–E. Although these speeds are similar to observed surface currents (e.g., Bryden and Brady 1985), they do not penetrate as deep and the westward transports of 8.5 and 7.8 Sv, respectively, are much less than Wyrtki and Kilonsky's (1984) SEC transport estimate. As expected in models of this class, the currents are too diffuse and eastward flow tends to cancel westward flow, but the overall near-zero transport does agree with the Wyrtki and Kilonsky (1984) estimates for all zonal flow within 9° of the equator and above 300 m.

The global impact of KPP on surface currents can be demonstrated clearly by comparing the annual means from B–K and B–E, because the wind driving and buoyancy boundary conditions are identical in the two cases. As seen at the equator (Fig. 14) the effect quickly diminishes with depth, so only the upper-level velocity components are shown in Fig. 15. A larger westward surface flow with KPP is evident across the equatorial Pacific, the equatorial Atlantic, and the Indian Ocean centered at 10°S. The eastward surface ACC is typically 2 cm s^{-1}, or 20% larger in B–K than in B–E. However, the zonal surface flow in the subtropical gyres of the Northern Hemisphere are very similar in the two cases.

The meridional currents at the surface also tend to be greater in B–K than B–E (Fig. 15). The northward flow from the ACC region is generally about 1 cm s^{-1} faster

in B–K, as is the southward flow in the subtropical gyres of the Southern Hemisphere, resulting in greater large-scale convergence. Meridional surface divergence across the equator is much larger in B–K. At 200°E, the difference in meridional currents between 5°N and 5°S is 16 cm s^{-1} in B–K and only 9 cm s^{-1} in B–E. In R–E and B–E, this divergence extends throughout the upper 50 m of enhanced mixing, but only to 30 or 40 m in the KPP variants. In all cases there is convergence below, which extends deeper in the Atlantic (300 m) than in the Pacific (200 m). These flows and the divergent zonal velocity fields (Fig. 14) produce equatorial upwelling everywhere (Fig. 11). Again, because of the resolution the upwelling velocities are small (less than 4×10^{-6} m s^{-1}) compared to the maximum Bryden and Brady (1985) estimate of 30×10^{-6} m s^{-1} at 70-m depth. Also noteworthy in Fig. 15 are the larger B–K surface currents in the upwelling regions off the west coasts of North America, South Africa, and South America.

6. Sensitivity to sea ice boundary conditions

Without a coupled sea ice model, bulk forcing cannot be applied under sea ice. Instead strong restoring is the dominant heat and freshwater forcing of (3.2) in regions of diagnosed sea ice. In certain situations the formation and melt of sea ice is another contributor to the forcing. The sensitivity of the bulk forcing results to these sea ice boundary conditions is now examined by comparing B–K to two other equilibrium solutions: B–K_1 and B–K_2. Recall that because of the apparent deeper mixing of KPP the restoring coefficients, Γ_Q and Γ_F of (3.1), of most bulk cases were chosen to be four times larger than those in the restoring cases (Table 1) in an attempt to keep similar restoring timescales and surface fluxes. Although the Arctic fluxes are more similar, a visual comparison of the high-latitude fluxes in Figs. 3 and 4 shows that this attempt results in considerably more small-scale spatial variability; particularly in the Arctic freshwater flux. Therefore, a valid and perhaps better choice would have been to keep these restoring coefficients the same in all cases. This option is examined in case B–K_1, which is identical to B–K in all respects, except that the strong, under-ice restoring coefficients are reduced to their R–E and R–K values (Table 1).

The effects of the reduced B–K_1 under-ice restoring strength on temperature and salinity distributions are discussed in section 5b. These and other effects are summarized as follows. The spatial variability seen in the Arctic surface fluxes of the B–K case (Figs. 3 and 4) is reduced in B–K_1 to be similar to that seen in the R–E case. The barotropic transports of both the ACC and North Atlantic subpolar gyre are weakened by about 10%. In the Weddell Sea region of the Antarctic, there is more freshwater input and less heat loss, which both contribute to a warmer, fresher, lighter AABW. With less density, the transport of AABW to abyssal depths is reduced. The NADW when formed appears to be warmer also, but more saline, so there are compensating effects on density. Figure 16 shows that the warmer water spreads to all depths and all ocean basins, making the B–K_1 case more like the Levitus (1982) climatology in this respect. This figure suggests also that the changed AABW properties and transport dominate the changes in deep salinity. In the global average the fresher water is found at all depths below about 1000 m, implying more vigorous mixing between AABW and NADW as they spread, perhaps because of the reduced density difference. In this respect the B–K_1 case is less like the Levitus climatology. There is little difference in the properties and extent of AAIW.

In B–K the heat and freshwater fluxes due to freezing and melting of sea ice (3.4) can occur anywhere. Although these fluxes represent a physical process, the implicit ice model is overly simple, with no transport of ice and a continuous accumulation of ice at some points. Therefore, a sensitivity experiment, B–K_2, is integrated with acceleration for 160 surface tracer years with $f_{si} = 0$ in (3.2) (Table 1), and starting at year 800 of the B–K accelerated integration. There is only a 6-yr synchronous integration for this case, and the results are annual-means for the last synchronous year. Without sea ice formation there is a 5% increase in the barotropic transports of both the ACC and North Atlantic subpolar gyre, and both the AABW and NADW become more saline and warmer (Fig. 16). This latter result implies that deep-water properties are affected most by ice melt. The melting ice of B–K tends to make the surface waters fresh and cold so that, when this water is advected to regions of deep-water formation as characterized by late winter deep boundary layers of Fig. 5, the global abyssal water ends up with a fresh, cold bias relative to B–K_2.

A comparison of Fig. 16 to Figs. 7 and 9 shows that the deep-water properties, especially salinity, are very sensitive to the under-ice restoring coefficient. The improved deep salinities of B–K over R–E are reduced by about 30% in B–K_1. Sea ice freeze and melt does have noticeable effects but is prevented from having its full impact under sea ice, where restoring provides the dominant heat and salt fluxes. This demonstrates sensitivity to ice fluxes, which cannot be addressed in a physically meaningful way without a coupled ice model.

7. Discussion and summary

As hypothesized, more realistic and less constraining surface boundary conditions, more physical subgrid-scale vertical mixing, and more accurate domain geometry and topography, compared to DM95 (Danabasoglu and McWilliams 1995), collectively result in improved equilibrium OGCM solutions. The most profound effects are due to the altered boundary conditions over the ice-free ocean, but the strength of the under-ice restoring exerts significant influence. The different subgrid-scale mixing has little effect on the annual-mean state of the model ocean, probably because the interior

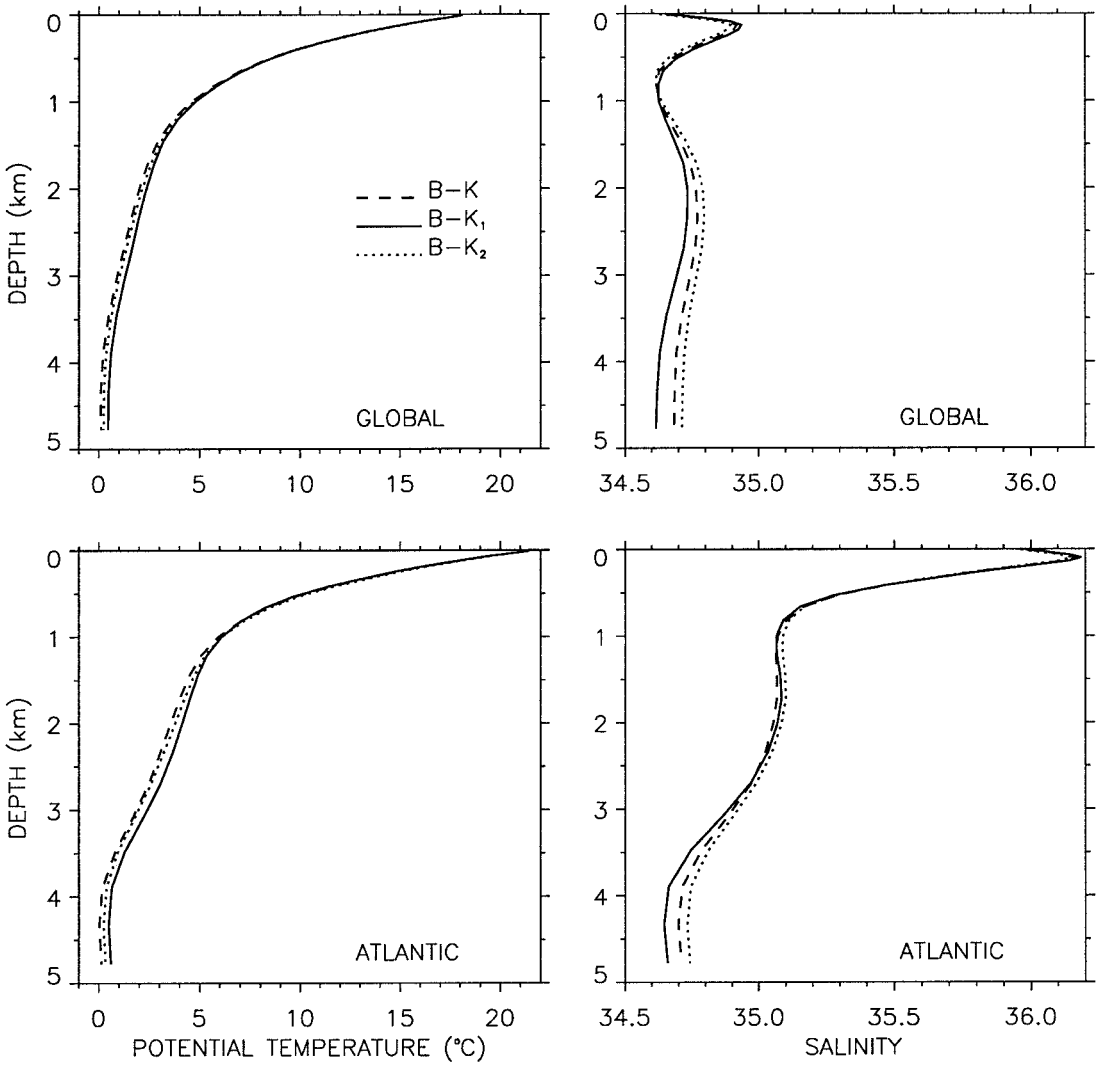

FIG. 16. Vertical profiles of the annual- and horizontal-mean potential temperature and salinity for B–K sensitivity experiments. In B–K_2, the annual-mean profiles are obtained over the sixth year of the synchronous integration.

diffusivities are similar in all cases. Significant impacts are confined to the upper few hundred meters and to mixed layer depths in regions of high-latitude deep convection. The effects of topography are generally confined locally, but are significant in some instances.

Seemingly small differences in otherwise acceptable equilibrium surface heat flux (Fig. 3) and freshwater flux (Fig. 4) fields produce major differences in model solutions. Throughout the course of an integration, the bulk forcing boundary conditions maintain the global average salinity much nearer the observed value than restoring boundary conditions (Fig. 2). This salt difference is mainly found below 1000 m (Fig. 9) where warmer, slightly improved temperatures are also found (Fig. 7). England (1993) showed that restoring boundary condition cases can be made to produce the more saline deep water if unphysical perpetual wintertime freshwater flux adjustments are made. These improvements in deep thermohaline properties are generally found in all basins at all latitudes (Figs. 8 and 10). The Atlantic salinity profile (Fig. 9) and zonal mean (Fig. 10) indicate that in the bulk forcing case B–K, the North Atlantic Deep Water is nearly 0.2 ppt more saline than observed and the Antarctic Bottom Water is more that 0.1 ppt too fresh. The excellent agreement with Levitus in the downstream basins (Fig. 9) appears to result from vertical mixing of these two water masses, but the change from a high salinity bias to a fresh bias around 3000-m depth persists.

The narrower and shallower Drake Passage appears to be the principal cause of the reduction in ACC barotropic transport, relative to DM95, and it may even be related to the increase of the Indonesian Throughflow, which has an excessively wide passage in both configurations. Much less of these observed changes were due to the different wind stress climatologies. The increased

resolution and the different wind stress do give larger western boundary current transports than reported by DM95. However, allowing the Kuroshio access in and out of the Sea of Japan through unrealistically deep (1000 m) wide channels (200 km) has resulted in far too much flow (14 Sv) taking this route. As a consequence of the warm water north and west of the model's island of Japan, this region is the site of too much surface cooling (Fig. 3) and freshwater loss (Fig. 4), and the region of large cooling and evaporation does not penetrate far enough into the North Pacific. Realistic ocean bottom topography between Greenland and Europe locks the position of the sinking branch of the Atlantic thermohaline circulation to the Icelandic Ridge. With a deeper ridge (e.g., 2500 m as in DM95), the sinking occurs about 10° north of the ridge, the warm northward surface flow appears to transport too much heat to these latitudes, and the Atlantic meridional overturning circulation is somewhat stronger. Thus, we conclude, as others before, that the necessary but somewhat arbitrary choices about grid-scale domain geometry have nontrivial consequences for the solutions.

Bulk forcing more than compensates for the shallow, more realistic Icelandic Ridge by increasing the maximum meridional streamfunction in the North Atlantic from less than 17 Sv in R–E and R–K to more than 22 Sv in B–E and B–K (Fig. 11). In these latter bulk cases the northward heat transport in the Atlantic, Indo–Pacific, and hence global basins is consistent with most ocean observational and inverse estimates, including the recent global inverse estimates of Macdonald and Wunsch (1996). The most notable exceptions are their estimates at 10°S and 10°N, which may be in error by more than the uncertainties ascribed to them. There are unacceptably large differences, however, with the Trenberth and Solomon (1994) atmospheric residual estimates, especially in the Indo–Pacific and South Atlantic subtropics (Fig. 12). Similar residual calculations based on NCEP reanalyses are showing better agreement with the model and other observational heat transports (K. Trenberth 1997, personal communication). Deviations of bulk forced solutions from the restoring cases are largest in the North Atlantic and in the same sense in the Indo–Pacific. Unfortunately, the various estimates of oceanic heat transport do not provide a tight enough constraint on model performance.

Model to model differences in oceanic freshwater transport (Fig. 13) are comparable to differences with the surface flux-based estimates of Wijffels et al. (1992). Deficiencies in the models, in the bulk forcing, and in the observational estimates are likely all contributors. The meridional gradients, and hence the fluxes, of the B–K global freshwater transport (Fig. 13) are generally in agreement with Wijffels et al. (1992), with the exception of the ITCZ and storm track regions. In contrast, the R–E distributions display more widespread dissimilarities in the meridional gradients, especially in the Northern Hemisphere. This result implies that the Fig. 4 differences between the R–E and B–K net surface freshwater fluxes are significant.

As hoped, the KPP vertical mixing scheme produces mixed layers and boundary layers with realistically large temporal and spatial variability (Fig 5). Figure 2 does show B–K to have improved global average salinity and temperature over B–E. However, the overall biases in vertical profiles (Fig. 7 and Fig. 9) are very similar in the two cases. Enhanced mixing in B–E forces all quantities to be uniform throughout all model layers above 50-m depth; with KPP, however, there can be significant differences between any two adjacent layers, even when those layers are both within the mixed layer (Large et al. 1994). This feature is particularly evident in the equatorial oceans where the westward surface velocity with KPP is typically twice as fast as when enhanced 50-m mixing is used. Generally faster surface currents and more intense surface convergence and divergence are found all over the global oceans in solutions that use KPP (Fig. 15).

Even though the B–K equilibrium solution displays some marked improvements over DM95, there are still some major blemishes. Most important of these would seem to be the formation and distribution of NADW and AABW. The former does not penetrate deep enough, as is typical of models of this class, and the problem may lie either with the numerics, the model physics, or the boundary conditions, though we believe it is likely that all three contribute. A related major concern is the unacceptably large sensitivity to the under sea ice restoring coefficient and to sea ice formation and melt. This problem may be overcome by coupling the ocean model to a prognostic sea ice model with both dynamics and thermodynamics. The unphysical and arbitrary restoring boundary conditions could then be replaced with bulk forcing with suitable modifications due to the presence of any sea ice, and the negative feedbacks of such modifications and advection by the dynamics should prevent the continuous accumulation of sea ice both locally and globally.

Acknowledgments. We would like to thank Dr. Peter R. Gent for helpful discussions and suggestions. We greatfully acknowledge the programming support of Jan Morzel during various stages of this work. GD was supported by the NOAA Office of Global Programs under Grant NA56GP0246. The National Center for Atmospheric Research is sponsored by the National Science Foundation.

APPENDIX A

Surface Forcing Fields

Complete specification of bulk surface boundary conditions (section 3) requires global fields of the following: the zonal and meridional wind stress components (τ_x and τ_y), the air temperature T_a, and specific humidity

TABLE A1. Data sources used to construct the prescribed atmospheric state for bulk surface forced cases.

	Variable	Source	Original time interval
U_{10}	Zonal wind component	NCEP	6 h
V_{10}	Meridional wind component	NCEP	6 h
T_a	Air temperature	NCEP	6 h
q_a	Specific humidity	NCEP	6 h
C	Cloud fraction	ISCCP	daily
Q_{sw}	Surface insolation	ISCCP	daily
P	Precipitation	MSU	monthly

q_a, the fractional cloud cover C, the net downward shortwave radiation Q_{sw}, the Shea et al. (1990) sea surface temperature θ_{STR}, and the Levitus (1982) upper-ocean salinity S_L. In each case 12 mean monthly fields are generated either from data covering the four years 1985 through 1988 or from climatologies (θ_{STR} and S_L), then bilinearly interpolated to the model grid. From these fields, the 12 ''midmonth'' surface fields are constructed so that linear interpolation to each model time step preserves the monthly means. This problem is reduced to a single tridiagonal matrix inversion by requiring that the interpolated values at the start and end of a time series both equal the arithmetic mean of the first and last monthly values.

The S_L fields are averages over the upper 4 levels (50 m) of the monthly ocean salinity climatology of Levitus (1982) but, because only seasonal values are available, linear interpolation is used to produce monthly S_L fields. The fractional coverage of sea ice f_{ice} is diagnosed from θ_{STR} as

$$f_{\text{ice}} = \begin{cases} 1, & \theta_{STR} \le \theta_f \\ \theta_{STR} - \theta_f, & \theta_f < \theta_{STR} < \theta_f + 1.0^\circ\text{C} \\ 0, & \theta_f + 1.0^\circ\text{C} \le \theta_{STR}, \end{cases} \tag{A.1}$$

where the approximate freezing point of sea water, $\theta_f = -1.8^\circ$C, is used in the climatology to indicate the presence of sea ice.

a. Bulk air–sea flux formulations

Table A1 lists the data sources used to construct the prescribed atmospheric state required for bulk air–sea forcing. The NCEP reanalysis data includes four times daily (0000, 0600, 1200, 1800 UTC) values of zonal U_{10}, and meridional V_{10} 10-m winds and surface 2-m T_a and q_a (Kalnay et al. 1996). The wind stress components are computed from the four times daily data using the bulk formulae:

$$\tau_x = \rho_a C_D U_{10} W_{10},$$
$$\tau_y = \rho_a C_D V_{10} W_{10}, \tag{A.2}$$

with a wind-speed-dependent empirical drag coefficient C_D corrected for atmospheric surface layer stability (e.g., Large et al. 1994; NCAR Oceanography Section 1996). The term W_{10} is the 10-m wind speed [$W_{10} = (U_{10}^2 + V_{10}^2)^{1/2}$] and ρ_a is the air density. The 12 mean monthly, and hence midmonth, fields are all derived from the four times daily values of τ_x, τ_y, W_{10}, T_a, and q_a.

The turbulent heat fluxes are computed from interpolated midmonth atmospheric fields using standard air–sea transfer equations (Large and Pond 1982):

$$Q_{\text{sen}} = \rho_a c_p^a C_H W_{10}(T_a - \theta_1), \tag{A.3}$$

$$Q_{\text{lat}} = \rho_a L_e C_E W_{10}(q_a - q_1), \tag{A.4}$$

where c_p^a and L_e are the specific heat of air and latent heat of vaporization and θ_1 and q_1 are the sea surface temperature and implied saturated specific humidity from the model. The transfer coefficients for heat, C_H, and evaporation, C_E, are both corrected for atmospheric stability (Large et al. 1994; NCAR Oceanography Section 1996).

The net longwave radiation Q_{lw} is calculated from a conventional bulk radiation formula of Berliand and Berliand (Fung et al. 1984):

$$Q_{\text{lw}} = -\epsilon\sigma_{\text{SB}}\{T_a^4[0.39 - 0.05(e_a)^{0.5}]F(C) + 4T_a^3(\theta_1 - T_a)\}, \tag{A.5}$$

where e_a (mb) is the surface water vapor pressure found from the q_a fields, ϵ is the surface emissivity taken as 1.0 to account for reflected longwave radiation (Lind and Katsaros 1986), and σ_{Sb} is the Stefan–Boltzmann coefficient equal to 567×10^{-10} W m^{-2} K^{-4}. The effect of clouds on the longwave flux is parameterized with a cloud correction factor $F(C)$ following Budyko (1974):

$$F(C) = 1 - a_c C^2, \tag{A.6}$$

where the cloud fraction C varies from 0 to 1.0 and a_c is a latitude-dependent empirical coefficient adapted by Fung et al. (1984) from Bunker (1976). The cloud fraction data are from the ISCCP C1 dataset (Rossow and Schiffer 1991). The ISCCP cloud data coverage is poor in winter high latitudes because of low insolation and missing geosynchronus satellite data. The local annual-mean is used to fill in missing data for regions with partial coverage. For a few areas, in particular the Indian sector of the Southern Ocean, the cloud fraction data is recomputed from the Bishop and Rossow (1991) surface clear and total insolation data using zonal-mean linear regressions between C and the ratio clear sky to total insolation.

The presence of clouds has an opposite and partially compensating effect on longwave (warming) and shortwave (cooling) forcing of the ocean surface, so it is important to have a consistent treatment of clouds for both radiative components. Bishop and Rossow (1991) present an algorithm, based on a one-dimensional atmospheric radiative transfer model, for computing surface shortwave irradiance from the ISCCP cloud data

on the same grid as the C1 cloud data. The daily mean surface insolation from Version 2 (Bishop et al. 1997) is used here, and a constant albedo of 7% is applied to the downward shortwave flux to compute Q_{sw}. Shortwave radiation is allowed to penetrate below the model surface leading to subsurface bulk heating. The subsurface profile for shortwave radiation is computed with the two-band approximation of Paulson and Simpson (1977) with a uniform Jerlov water type Ib.

Evaporation is given directly from Q_{lat} of (A.4) by dividing by L_e. Monthly precipitation (Table A1) estimates from the MSU satellite analysis (Spencer 1993) are used to form midmonth climatologies as above. These MSU data P_{MSU} have been calibrated against coastal and island rain gauge data. However, averaged over the ocean the annual-mean MSU precipitation is 10%–30% lower than given by other (e.g., Legates and Willmott 1990) climatologies (D. Shea 1996, personal communication). The MSU precipitation data is limited to 60°S to 60°N, and the high latitude regions are filled with the monthly, zonal average precipitation values from either 60°S or 60°N.

b. Balancing the annual heat and freshwater fluxes

The atmospheric climatology used for the bulk forcing integrations has been adjusted, within acceptable error ranges, to generate a globally balanced heat and freshwater budget for the ocean with a realistic model sea surface temperature. When the heat fluxes are computed as outlined above using Shea et al. (1990) sea surface temperatures, the global average net heat flux is $+43.2$ W m^{-2} (Table 2). Before an annual balance could be achieved the uncoupled ocean surface temperatures would need to increase by about 1°C. In order to achieve a balance with realistic surface temperatures the solar radiation and q_a are decreased as described below. An even larger adjustment, by about 8 W m^{-2}, would be required if C, rather than C^2, were used in (A.6).

The Bishop and Rossow (1991) data show generally good agreement with long-term weathership surface irradiance climatologies (e.g., Dobson and Smith 1988), with a positive bias of 10–20 W m^{-2} in the ISCCP estimates at some stations (Bishop et al. 1997). This bias is only one of a growing number of empirical indications (including comparisons with land stations) that radiative transfer equations transmit too much solar radiation to the surface (J. Kiehl 1996, personal communication). It is crudely accounted for by uniformly multiplying the solar radiation by a factor 0.875.

Kent and Taylor (1995) produce an annual cycle of latent heat flux for a portion of the midlatitude North Atlantic using corrected observations from a select subset of North Atlantic Volunteer Observing Ships (VOS). Their annual cycle has systematically more negative latent heat flux by 10–20 W m^{-2} than the corresponding cycle from the NCEP data and Shea et al. (1990) surface temperatures. This difference is too large to be attributed to uncertainties in the wind speed and the transfer coefficient. However, the two annual cycles are brought into good agreement by multiplying the NCEP 2-m specific humidity by a uniform factor of 0.93. This drying adjustment may reflect a tendency for model assimilated ocean humidity observations from VOS to be too moist (Kent et al. 1993). An inability of the NCEP model boundary layer to remove sufficient moisture upward from the surface is also a potential contributor.

This adjustment of q_a results in more latent (A.4) and longwave (through e_a in A.5) cooling, and more freshwater loss by evaporation (Table 1). A global balance between evaporation and precipitation is then attained by multiplying P_{MSU} by a uniform precipitation adjustment factor $f_P = 1.132$. The resulting precipitation then becomes more like other climatologies.

However, the precipitation needed to balance evaporation using θ_{STR} does not balance evaporation computed using evolving upper model layer temperature. Therefore, a precipitation correction factor $f_P(y)$ is computed for each year y of the model integration. The precipitation throughout year y is given by

$$P = f_P(y)P_{MSU}. \tag{A.7}$$

The correction factor is increased for the next year, $y + 1$, if the annual change in globally averaged salinity $\Delta\langle S\rangle_y$ is positive and it is decreased if model salinity decreases. This change is multiplied by a constant factor $-\rho_o S_o^{-1} V_o$ (where V_o is the model ocean volume and $S_o = 34.7$ psu is the ocean reference salinity) to give the equivalent change in the mass of global ocean freshwater ΔM_y^F. The mass of MSU precipitation falling on the ice free ocean during a year, M_{MSU}^P, is the annual integral of the globally integrated P_{MSU} times the ice free ocean area. At the end of each year these quantities are used to compute

$$f_P(y + 1) = f_P(y)\left(1 - \frac{\Delta M_y^F}{f_P(y)M_{MSU}^P}\right), \tag{A.8}$$

where during the first year $f_P(1) = 1.100$. In B–K (B–E), globally averaged salinity decreases over each of the first two years of integration, making $f_P(2) = 1.059$ (1.009) and $f_P(3) = 1.055$ (1.050). Salinity then generally increases for about 200 surface tracer years. For the remainder of the accelerated integration, changes in $\Delta\langle S\rangle_y$ are small and the precipitation factor remains approximately constant at $f_P(y) = 1.105$ (1.108). A constant factor with this value is used throughout the synchronous integration (Table 1).

Insofar as the precipitation correction and the weak restoring are accounting for errors in P_{MSU}, but neither model salt transport deficiencies nor errors in evaporation, then the effective precipitation seen by the model is the sum of $f_P(y)\ P_{MSU}$ and F_w. Near coasts the weak restoring includes river runoff from precipitation over

land, so there is no explicit river runoff in the model forcing.

APPENDIX B

Tapering of the Isopycnal and Thickness Diffusivities

In isopycnal mixing parameterizations, an important variable is **S**, defined as negative the nondimensional ratio of the horizontal density gradient vector to the scalar vertical density gradient. These parameterizations are applied only in stable stratification, so the isopycnal slope is defined as $|\mathbf{S}|$. When this slope becomes excessively steep, the mixing can create numerical instabilities (Cox 1987; Hirst and McDougall 1996). To overcome this problem, an approach limiting the slope to be less than a maximum value ($S_{\max}$) has been widely used in the Redi (1982)–Cox (1987) isopycnal mixing parameterization, in spite of the major disadvantage that spurious diapycnal diffusion for slopes steeper than $S_{\max}$ is produced. In most cases DM95 also uses this approach with $S_{\max} = 0.01$ for the Gent and McWilliams (1990) isopycnal transport parameterization. In a recent implementation of this parameterization, Hirst and McDougall (1996) choose to use the maximum slope limit approach with $S_{\max}$ as a function of depth and set $S_{\max} = 0.002$ near the surface. This choice of $S_{\max}$ also limits the eddy-induced transport velocity magnitudes, especially near the surface. A discussion of similar stability problems pertaining to the Redi–Cox parameterization and a method for tapering of A_I while preserving the computed isopycnal slopes can be found in Gerdes et al. (1991).

Our investigations with a finer vertical resolution (12 m) than DM95 (50 m) near the ocean surface show that the near-surface mixing tensor elements, and hence the isopycnal advection velocity, can become excessively large due to diminished vertical density gradients. Also, especially near the ocean surface, the isopycnal transport parameterization and the KPP vertical mixing scheme conflict. While the latter works to make isopycnals vertical, the former strives to flatten the isopycnals (Gent et al. 1995) and dominates more than the observations of mixed layer depth indicate. To ameliorate these problems in the present investigation we chose to use two tapering functions.

The method is essentially based on smoothly tapering both A_I and A_{ITD} to zero as either the isopycnal slope becomes large or the ocean surface is approached. It is expressed as

$$A_I = f_1 f_2 A_I \quad \text{and} \quad A_{ITD} = f_1 f_2 A_{ITD}, \tag{B.1}$$

where the f_1 function is shown in Fig. B1 and is the same as the f function detailed in Eq. (A.7) of DM95. As shown in Fig. B1, it reduces A_I and A_{ITD} by 50% when the isopycnal slope reaches a critical value, $S_c = 0.004$, while the abruptness of the tapering is controlled by a parameter $S_d = 0.001$. Both A_I and A_{ITD} are zero for $|\mathbf{S}| > S_{\max} = 0.01$. In contrast to the maximum slope limit approach, this method eliminates any spurious diapycnal diffusion, because mixing always operates along the computed slopes.

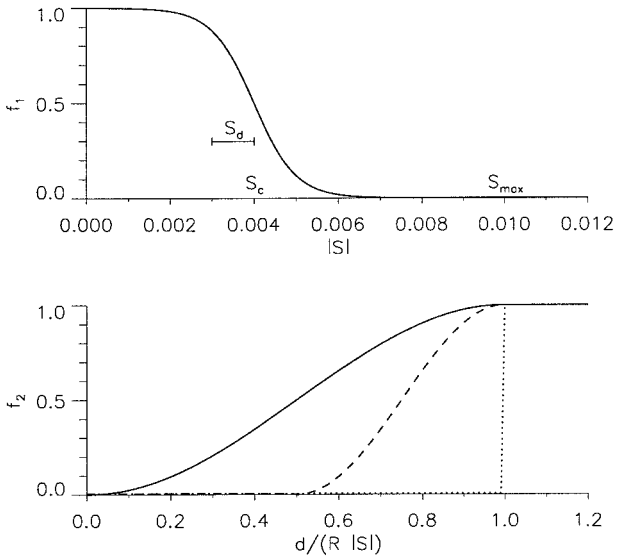

FIG. B1. Tapering functions used for A_I and A_{ITD} in Eq. (B.1). In the bottom panel, the dotted and dashed lines show the f_2 distributions used in the f_2 sensitivity experiments.

The second function f_2 is designed to reduce the isopycnal mixing near the ocean surface if the isopycnal slopes are too large, thus limiting the competition with vertical mixing. Here, the idea is to compare the water parcel depth d with the vertical displacement distance D associated with a horizontal displacement equivalent to the Rossby radius of deformation R. Because this radius represents the preferred horizontal length scale of the baroclinic eddies, the vertical displacement is given by

$$D = R\,|\mathbf{S}|, \tag{B.2}$$

where usually $|\mathbf{S}| \ll 1$. The governing parameter becomes the ratio

$$r = \frac{d}{D}. \tag{B.3}$$

A parcel traveling isopycnally can cover its full horizontal displacement without reaching the surface only for values of r greater than unity. For values of r less than unity the supposed encounter with the surface presumably reduces the isopycnal mixing. Consequently, we construct the f_2 function for $r < 1$ as follows:

$$f_2 = \frac{1}{2}\left[1 + \sin\pi\left(r - \frac{1}{2}\right)\right]. \tag{B.4}$$

Our investigations show that the model solutions are not sensitive to the specifics of the f_2 function. The forms used in two f_2 sensitivity experiments (dotted and

dashed lines) and in the present cases (solid line) are given in Fig. B1.

In (B.2), the Rossby radius is determined from

$$R = \frac{c}{f}, \tag{B.5}$$

with $c = 2$ m s^{-1} is the first baroclinic wave speed, and $f = 2\Omega \sin\phi$ is the Coriolis parameter, where Ω is the angular velocity of the earth and ϕ is latitude. An additional restriction is 15 km $\leq R \leq$ 100 km. Because $f_1 = 0$ for slopes larger than $S_{\max}$, the corresponding f_2 values are irrelevant. Note that the construction of f_2 is completely self-contained in the isopycnal transport parameterization scheme, and that it is not dependent on a vertical mixing parameterization.

REFERENCES

Anis, A., and J. N. Moum, 1992: The superadiabatic surface layer of the ocean during convection. *J. Phys. Oceanogr.,* **22,** 1221–1227.

Barnier, B., L. Siefridt, and P. Marchesiello, 1995: Surface thermal boundary condition for a global ocean circulation model from a three-year climatology of ECMWF analyses. *J. Mar. Res.,* **6,** 363–380.

Baumgartner, A., and E. Reichel, 1975: *The World Water Balance.* Elsevier, 179 pp.

Bishop, J. K. B., and W. B. Rossow, 1991: Spatial and temporal variability of global surface solar irradiance. *J. Geophys. Res.,* **96,** 16 839–16 858.

——, ——, and E. G. Dutton, 1997: Surface solar irradiance from the international Satellite Cloud Climatology project 1983–1991. *J. Geophys. Res.,* **102,** 6883–6910.

Bryan, F. O., 1987: Parameter sensitivity of primitive equation ocean general circulation models. *J. Phys. Oceanogr.,* **17,** 970–985.

——, and A. Oort, 1984: Seasonal variation of the global water balance based on aerological data. *J. Geophys. Res.,* **89,** 11 717–11 730.

——, B. G. Kauffman, W. G. Large, and P. R. Gent, 1996: The NCAR CSM flux coupler. NCAR Tech. Note NCAR/TN-424+STR, 50 pp. [Available from NCAR, P. O. Box 3000, Boulder, CO 80303.]

Bryan, K., 1969: A numerical method for the study of the circulation of the world ocean. *J. Comput. Phys.,* **4,** 347–376.

——, 1984: Accelerating the convergence to equilibrium of ocean–climate models. *J. Phys. Oceanogr.,* **14,** 666–673.

——, 1991: Ocean circulation models. *Strategies for Future Climate Research,* M. Latif, Ed., Max-Planck-Institut für Meteorologie, 265–286.

Bryden, H. L., and E. C. Brady, 1985: Diagnostic model of the three-dimensional circulation in the upper equatorial Pacific Ocean. *J. Phys. Oceanogr.,* **15,** 1255–1273.

——, D. H. Roemmich, and J. A. Church, 1991: Ocean heat transport across 24°N in the Pacific. *Deep-Sea Res.,* **38,** 297–324.

Budyko, M. I., 1974: *Climate and Life.* Vol. 18, *International Geophysics Series,* Academic Press, 508 pp.

Bunker, A. F., 1976: Computation of surface energy flux and annual air–sea cycle of the North Atlantic Ocean. *Mon. Wea. Rev.,* **104,** 1122–1140.

Chen, D., A. J. Busalacchi, and L. M. Rothstein, 1994: The roles of vertical mixing, solar radiation, and wind stress in a model simulation of the sea surface temperature seasonal cycle in the tropical Pacific Ocean. *J. Geophys. Res.,* **99,** 20 345–20 359.

Cox, M. D., 1984: A primitive equation, 3-dimensional model of the ocean. GFDL Ocean Group Tech. Rep. No. 1, 143 pp. [Available from GFDL, Princeton, NJ 08542.]

——, 1987: Isopycnal diffusion in a z-coordinate ocean model. *Ocean Modelling* (unpublished manuscripts), **74,** 1–5.

——, and K. Bryan, 1984: A numerical model of the ventilated thermocline. *J. Phys. Oceanogr.,* **14,** 674–687.

Danabasoglu, G., and J. C. McWilliams, 1995: Sensitivity of the global ocean circulation to parameterizations of mesoscale tracer transports. *J. Climate,* **8,** 2967–2987.

——, ——, and P. R. Gent, 1994: The role of mesoscale tracer transports in the global ocean circulation. *Science,* **264,** 1123–1126.

——, ——, and W. G. Large, 1996: Approach to equilibrium in accelerated global oceanic models. *J. Climate,* **9,** 1092–1110.

Derber, J. C., 1987: A conjugate gradient solution algorithm for the elliptical equation in the Cox–Bryan ocean model. GFDL Tech. Rep., 10 pp. [Available from GFDL, Princeton, NJ 08542.]

Dobson, F. W., and S. D. Smith, 1988: Bulk models of solar radiation at sea. *Quart. J. Roy. Meteor. Soc.,* **114,** 165–182.

England, M. H., 1993: Representing the global-scale water masses in ocean general circulation models. *J. Phys. Oceanogr.,* **23,** 1523–1552.

Fieux, M., C. Andrié, P. Delecluse, A. G. Ilahude, A. Kartavtseff, F. Mantisi, R. Molcard, and J. C. Swallow, 1994: Measurements within the Pacific–Indian Oceans throughflow region. *Deep-Sea Res.,* **41,** 1091–1130.

Freeland, H. J., P. B. Rhines, and H. T. Rossby, 1975: Statistical observations of the trajectories of neutrally buoyant floats in the North Atlantic. *J. Mar. Res.,* **33,** 383–404.

Fung, I. Y., D. E. Harrison, and A. A. Lacis, 1984: On the variability of the net long-wave radiation at the ocean surface. *Rev. Geophys. Space Phys.,* **22,** 177–193.

Gent, P. R., and J. C. McWilliams, 1990: Isopycnal mixing in ocean circulation models. *J. Phys. Oceanogr.,* **20,** 150–155.

——, and ——, 1996: Eliassen–Palm fluxes and the momentum equations in non-eddy-resolving ocean circulation models. *J. Phys. Oceanogr.,* **26,** 2539–2546.

——, J. Willebrand, T. J. McDougall, and J. C. McWilliams, 1995: Parameterizing eddy-induced tracer transports in ocean circulation models. *J. Phys. Oceanogr.,* **25,** 463–474.

Gerdes, R., C. Köberle, and J. Willebrand, 1991: The influence of numerical advection schemes on the results of ocean general circulation models. *Climate Dyn.,* **5,** 211–226.

Godfrey, J. S., 1989: A Sverdrup model of the depth-integrated flow for the World Ocean allowing for island circulations. *Geophys. Astrophys. Fluid Dyn.,* **45,** 89–112.

Gould, W. J., J. Loynes, and J. Backhaus, 1985: Seasonality in slope current transports northwest of Shetland. *ICES, Hydrogr. Committee C. M. 1985/C,* **7,** 13 pp.

Hall, M. M., and H. L. Bryden, 1982: Direct estimates and mechanisms of ocean heat transport. *Deep-Sea Res.,* **29,** 339–359.

Han, Y.-J., 1984: A numerical world ocean general circulation model. Part II: A baroclinic experiment. *Dyn. Atmos. Oceans,* **8,** 141–172.

Haney, R. L., 1971: Surface thermal boundary condition for ocean circulation models. *J. Phys. Oceanogr.,* **1,** 241–248.

Hirst, A. C., and J. S. Godfrey, 1993: The role of Indonesian Throughflow in a global ocean GCM. *J. Phys. Oceanogr.,* **23,** 1057–1086.

——, and W. Cai, 1994: Sensitivity of a world ocean GCM to changes in subsurface mixing parameterization. *J. Phys. Oceanogr.,* **24,** 1256–1279.

——, and T. J. McDougall, 1996: Deep-water properties and surface buoyancy flux as simulated by a z-coordinate model including eddy-induced advection. *J. Phys. Oceanogr.,* **26,** 1320–1343.

Hogg, N. G., 1992: On the transport of the Gulf Stream between Cape Hatteras and the Grand Banks. *Deep-Sea Res.,* **39,** 1231–1246.

Holloway, J. L., M. J. Spelman, and S. Manabe, 1973: Latitude–longitude grid suitable for numerical time integration of a global atmospheric model. *Mon. Wea. Rev.,* **101,** 69–78.

Kalnay, E., M. Kanamitsu, R. Kistler, W. Collins, D. Deaven, L. Gandin, M. Iredell, S. Saha, G. White, J. Woollen, Y. Zhu,

M.-Chelliah, W. Ebisuzaki, W. Higgins, J. Janowiak, K. C. Mo, C. Ropelewski, A. Leetmaa, R. Reynolds, and R. Jenne, 1996: The NCEP/NCAR 40-year reanalysis project. *Bull. Amer. Meteor. Soc.,* **77,** 437–471.

Kent, E. C., and P. K. Taylor, 1995: A comparison of sensible and latent heat flux estimations for the North Atlantic Ocean. *J. Phys. Oceanogr.,* **25,** 1530–1549.

——, ——, B. S. Truscott, and J. S. Hopkins, 1993: The accuracy of voluntary observing ships' meteorological observations—Results from the VSOP-NA. *J. Atmos. Oceanic Technol.,* **10,** 591–608.

Large, W. G., and S. Pond, 1982: Sensible and latent heat flux measurements over the oceans. *J. Phys. Oceanogr.,* **12,** 464–482.

——, J. C. McWilliams, and S. C. Doney, 1994: Oceanic vertical mixing: A review and a model with a nonlocal boundary layer parameterization. *Rev. Geophys.,* **32,** 363–403.

Larsen, J. C., 1992: Transport and heat flux of the Florida Current at 27°N derived from cross-stream voltages and profiling data: Theory and observations. *Philos. Trans. Roy. Soc. London A,* **338,** 169–236.

LeGates, D. R., and C. J. Willmott, 1990: Mean seasonal and spatial variability in gauge-corrected, global precipitation. *Int. J. Climatol.,* **10,** 111–127.

Levitus, S., 1982: *Climatological Atlas of the World Ocean.* NOAA Prof. Paper 13, U.S. Department of Commerce, 173 pp.

Lind, R. J., and K. B. Katsaros, 1986: Radiation measurements and model results from R/V Oceanographer during STREX 1980. *J. Geophys. Res.,* **91,** 13 308–13 314.

Macdonald, A. M., and C. Wunsch, 1996: An estimate of global ocean circulation and heat fluxes. *Nature,* **382,** 436–439.

McWilliams, J. C., 1996: Modeling the oceanic general circulation. *Annu. Rev. Fluid Mech.,* **28,** 215–248.

——, and Coauthors, 1983: The local dynamics of eddies in the Western North Atlantic. *Eddies in Marine Science,* A. R. Robinson, Ed., Springer-Verlag, 92–113.

Moisan, J. R., and P. P. Niiler, 1997: The seasonal heat budget of the North Pacific: Net heat flux and heat storage rates [1950–1990]. *J. Phys. Oceanogr.,* in press.

Molinari, R. L., E. Johns, and J. F. Festa, 1990: The annual cycle of meridional heat flux in the Atlantic Ocean at 26.5°N. *J. Phys. Oceanogr.,* **20,** 476–482.

Munk, W. H., 1950: On the wind-driven ocean circulation. *J. Meteor.,* **7,** 79–93.

NCAR Oceanography Section, 1996: The NCAR CSM Ocean Model. NCAR Tech. Note NCAR/TN-423+STR, 84 pp. [Available from NCAR, P. O. Box 3000, Boulder, CO 80303.]

Oberhuber, J. M., 1988: An atlas based on the 'COADS' data set: The budget of heat, buoyancy and turbulent kinetic energy at the surface of the global ocean. Max-Plank-Institute für Meteorology Rep. 15, 20 pp.

——, 1993: Simulation of the Atlantic circulation with a coupled sea ice-mixed layer-isopycnal general circulation model. Part I: Model description. *J. Phys. Oceanogr.,* **23,** 808–829.

O'Brien, J. J., 1970: A note on the vertical structure of the eddy exchange coefficient in the planetary boundary layer. *J. Atmos. Sci.,* **27,** 1213–1215.

Pacanowski, R. C., K. Dixon, and A. Rosati, 1991, 1993: The GFDL modular ocean model users guide. GFDL Ocean Group Tech. Rep. 2, GFDL, Princeton, NJ.

Paulson, C. A., and J. J. Simpson, 1977: Irradiance measurements in the upper ocean. *J. Phys. Oceanogr.,* **7,** 952–956.

Peterson, R. G., and L. Stramma, 1991: Upper-level circulation in the South Atlantic Ocean. *Progress in Oceanography,* Vol. 26, Pergamon Press, 1–73.

Redi, M. H., 1982: Oceanic isopycnal mixing by coordinate rotation. *J. Phys. Oceanogr.,* **12,** 1154–1158.

Rix, N. H., and J. Willebrand, 1996: Parameterization of mesoscale eddies as inferred from a high-resolution circulation model. *J. Phys. Oceanogr.,* **26,** 2281–2285.

Roemmich, D., and C. Wunsch, 1985: Two transatlantic sections: Meridional circulation and heat flux in the subtropical North Atlantic Ocean. *Deep-Sea Res.,* **32,** 619–664.

Rosati, A., and K. Miyakoda, 1988: A general circulation model for upper ocean simulation. *J. Phys. Oceanogr.,* **18,** 1601–1626.

Rossow, W. B., and R. A. Schiffer, 1991: ISCCP cloud data products. *Bull. Amer. Meteor. Soc.,* **72,** 2–20.

Salmon, R., 1990: The thermocline as an ''internal boundary layer.'' *J. Mar. Res.,* **48,** 437–469.

Schmitt, R. W., 1994: The ocean freshwater cycle. CCCO-JSC Ocean Observing System Development Panel, Texas A&M University, College Station, TX, 32 pp.

Shea, D. J., K. E. Trenberth, and R. W. Reynolds, 1990: A global monthly sea surface temperature climatology. NCAR Tech. Note NCAR/TN-345, 167 pp.

Sloss, P. W., 1988: Digital relief of the surface of the earth. Data Announcement 88-MGG-02, NOAA, National Geophysical Data Center, Boulder, CO.

Spencer, R. W., 1993: Global oceanic precipitation from the MSU during 1979–91 and comparisons to other climatologies. *J. Climate,* **6,** 1301–1326.

Stramma, L., and J. R. E. Lutjeharms, 1997: The flow field of the subtropical gyre of the South Indian Ocean. *J. Geophys. Res.,* **102,** 5513–5530.

Toggweiler, J. R., K. Dixon, and K. Bryan, 1989: Simulations of radiocarbon in a coarse-resolution World Ocean model 1. Steady state prebomb distributions. *J. Geophys. Res.,* **94,** 8217–8242.

Trenberth, K. E., and A. Solomon, 1994: The global heat balance: Heat transports in the atmosphere and ocean. *Climate Dyn.,* **10,** 107–134.

——, W. G. Large, and J. G. Olson, 1990: The mean annual cycle in global ocean wind stress. *J. Phys. Oceanogr.,* **20,** 1742–1760.

Tziperman, E., J. R. Toggweiler, Y. Feliks, and K. Bryan, 1994: Instability of the thermohaline circulation with respect to mixed boundary conditions: Is it really a problem for realistic models? *J. Phys. Oceanogr.,* **24,** 217–232.

Wajsowicz, R. C., 1993: A consistent formulation of the anisotropic stress tensor for use in models of the large scale ocean circulation. *J. Comput. Phys.,* **105,** 333–338.

Weller, R. A., and P. K. Taylor, 1993: Surface conditions and air-sea fluxes. CCCO-JSC Ocean Observing System Development Panel, Texas A&M University, College Station, TX, 131 pp.

Whitworth, T., III, 1983: Monitoring the transport of the Antarctic Circumpolar Current at Drake Passage. *J. Phys. Oceanogr.,* **13,** 2045–2057.

Wijffels, S. E., R. W. Schmitt, H. L. Bryden, and A. Stigebrandt, 1992: Transport of freshwater by the oceans. *J. Phys. Oceanogr.,* **22,** 155–162.

Wyngaard, J. C., 1982: Lectures on the planetary boundary layer. *Mesoscale Meteorology—Theories, Observations, and Models,* D. K. Lilly and T. Gal-Chen, Eds., NATO ASI Series, Ser. C, D. Reidel, 603–650.

Wyrtki, K., and B. Kilonsky, 1984: Mean water and current structure during the Hawaii-to-Tahiti shuttle experiment. *J. Phys. Oceanogr.,* **14,** 242–254.